The Hot Plasma and Radiation Environment of the Uranian Magnetosphere

B. H. Mauk,[1] S. M. Krimigis,[1] E. P. Keath,[1] A. F. Cheng,[1] T. P. Armstrong,[2] L. J. Lanzerotti,[3] G. Gloeckler,[4] and D. C. Hamilton[4]

We report on the hot plasma and particle radiation environment of the magnetosphere of Uranus as diagnosed with the low-energy charged particle investigation on the Voyager 2 spacecraft (measuring electrons and ions with energies $\gtrsim 22$ keV and $\gtrsim 28$ keV, respectively). The encounter of the inbound bow shock (at $\sim 24\ R_U$; $1\ R_U = 25{,}600$ km) was immediately preceded (~ 30–24 R_U) by intense upstream proton events characterized by bulk streaming pointing approximately tangentially to the magnetospheric boundaries (flowing away from the magnetospheric "nose" regions). Just inside a somewhat disturbed magnetopause, convective boundary layer flows were observed. Inside the magnetosphere proper the higher-energy particle channels ($\gtrsim 200$ keV) show dramatic evidence of losses associated with the planetary satellites. The positions of "flux minima" signatures within the electron channels are reasonably well ordered (but not exactly) by the predicted minimum L shell positions of the satellites. In contrast the proton signatures show larger deviations from such ordering, due at least in part to dynamical time variations. Excluding the magnetotail regions, the maximum observed hot plasma β parameter (β is particle pressure/magnetic pressure) was ~ 0.13, low by comparison with other visited magnetospheres. While the β parameter indicates that this magnetosphere is relatively "empty," the energetic electron fluxes in the inner regions nevertheless exceed the whistler mode stably trapped limit by 1 order of magnitude. The energy spectral properties of both ions and electrons within the "core" or hard radiation magnetospheric regions are unusual and complex and are often not well characterized using the so-called kappa distribution or a simple, one-slope power law. The low-energy portions of the electron distributions ($E < 200$ keV) generally have a power law shape ($j \sim E^{-\gamma}$) with γ between 1 and 3. However, in the vicinity of the minimum L shell position of the satellite Miranda ($L_{\min} \sim 4.9\ R_U$) the distribution dramatically thermalizes to a Maxwellian with a temperature $kT \sim 30$ keV. The low-energy proton spectral shapes ($E < 200$ keV) vary between power law ($\gamma \sim 1.5$–4) and Maxwellian shapes ($kT \sim 35$–50 keV). Most unusual is the distinctly Maxwellian shape of the high-energy ions ($E \sim 200$–3500 keV) within several regions, with temperature parameters between 125 and 250 keV. At other locations a high-energy power law suffices (with $\gamma \sim 2.5$–4). The shapes of the core magnetospheric pitch angle distributions generally show well-developed trapped or "pancake" forms at both low and high energies. In the outbound trajectory between the minimum L shell locations of the satellites Miranda and Ariel there is evidence of a population confined particularly close to the magnetic equator, perhaps explaining an apparent dramatic inbound/outbound asymmetry in the flux profiles in this region of the magnetosphere. The magnetotail is very active for particles at low (~ 30 keV) energies. Substantial "plasma sheet" ion and electron enhancements were observed at the previously reported "neutral sheet" crossings. In addition, there were sporadic ion enhancements well separated in time and space from the neutral sheet. Also, dramatic field-aligned streaming of energetic particles was observed at the boundaries of these ion enhancements, reminiscent of the energetic particle streaming observed at the boundaries of the plasma sheet of the Earth's magnetotail. The streaming is sometimes in the planetward and sometimes in the tailward directions. These observations, together with the special properties of one particular plasma sheet encounter, are highly suggestive that substorm processes analogous to those occurring within the Earth's magnetotail are occurring within the Uranian magneotail. Furthermore, at least one energetic particle event observed within the quasi-dipolar regions was suggestive of substorm injection phenomena. We suggest that time-stationary convection models of particle transport be viewed with caution.

Introduction

The magnetosphere of Uranus has been shown, by means of instrumentation on the Voyager 2 spacecraft, to be a rich environment for the study of magnetospheric interactions (*Science* special issue, 233, July 4, 1986). In addition to the "standard" array of magnetospheric phenomena, ranging from upstream ion events, to the bow shock and magnetopause boundary structures, to an intense inner region of hard particle radiation, to a soft magnetotail plasma sheet population in the vicinity of the magnetotail neutral sheet, the mag-

netosphere of Uranus presents an unusual configuration with unique characteristics. As an example, the very large tilt of the magnetic dipole axis with respect to the planet's spin axis ($\sim 60°$ [*Ness et al.*, 1986]) means that the planetary satellites, traveling on orbits within a plane nearly perpendicular to the Sun-Uranus line, follow unusual paths in *B-L* space. It is perhaps surprising that the rather striking satellite-associated particle absorption signatures are as well ordered as they are [*Krimigis et al.*, 1986; *Stone et al.*, 1986].

Additionally unique to the Uranian magnetosphere is the relatively low value for the β (β is the ratio of particle pressure/magnetic pressure) of the plasma, which suggests that the magnetosphere of Uranus may resemble more closely historical concepts of what constitutes a magnetospheric configuration than do the other outer planets, even that of Earth [*Krimigis et al.*, 1986; *Bridge et al.*, 1986]. Also, the Uranian magnetospheric system has an almost complete absence of ions heavier than protons [*Krimigis et al.*, 1986; *Bridge et al.*, 1986] (H_2^{n+} is a very minor constituent). It is clear that the magnetosphere of Uranus will provide crucial data for comparative studies of magnetospheres.

[1] Applied Physics Laboratory, Johns Hopkins University, Laurel, Maryland.

[2] Department of Physics, University of Kansas, Lawrence.

[3] AT&T Bell Laboratories, Murray Hill, New Jersey.

[4] Department of Physics and Astronomy, University of Maryland, College Park.

TABLE 1. Voyager 2 LECP Channel Characteristics

Channel Designation	Species, Z	Effective Field of View, deg	Energy Passband,* MeV/nucleon	εG, cm^2 sr
Ion/Proton Channels				
PL01	$Z \geq 1$	45	0.028–0.043	1.13×10^{-1}
PL02	$Z \geq 1$	45	0.043–0.080	1.13×10^{-1}
PL03	$Z \geq 1$	45	0.080–0.137	1.13×10^{-1}
PL04	$Z \geq 1$	45	0.137–0.215	1.13×10^{-1}
PL05	$Z \geq 1$	45	0.215–0.540	1.13×10^{-1}
PL06	$Z \geq 1$	45	0.54–0.99	1.13×10^{-1}
PL07	$Z \geq 1$	45	0.99–2.14	1.13×10^{-1}
PL08	$Z \geq 1$	45	2.14–3.5	1.13×10^{-1}
39	$Z \geq 2$	60	0.035–0.069†	9.7×10^{-2}
38	$Z \geq 6$	60	0.069–0.20†	9.7×10^{-2}
32	$Z = 1$	60	0.33–0.61	2.6×10^{-3}
1	$Z = 1$	60	0.52–1.45	4.4×10^{-1}
33	$Z = 2$	60	0.23–0.48	9.7×10^{-2}
Electron Channels				
$E\beta 01$		45	0.022–0.035	6×10^{-3}
$E\beta 02$		45	0.035–0.061	6×10^{-3}
$E\beta 03$		45	0.061–0.112	6×10^{-3}
$E\beta 04$		45	0.112–0.183	3.9×10^{-3}
$E\beta 05$		45	0.183–0.5	2×10^{-3}
$E\gamma 06$		45	>0.252	8.1×10^{-3}‡
$E\gamma 07$		45	>0.480	3.5×10^{-3}‡
$E\gamma 08$		45	>0.853	1.7×10^{-4}‡
$E\gamma 09$		45	>1.20	

Note: this table shows only a subset (the most commonly used) of the channels available. Also, the "near-encounter" mode, which activates additional channels, was not used at Uranus.

*For $Z \geq 1$ channels, passband is given for protons only.

†Indicates oxygen passband.

‡εG for the difference between adjacent integral channels.

This paper, following the initial analysis presented by *Krimigis et al.* [1986], presents the first detailed account of the results of the Voyager 2 low-energy charged particle (LECP) investigation of the Uranian magnetosphere. The LECP instrument utilizes a variety of solid-state detectors to obtain measurements of electrons (22 keV $\leq E_e \leq$ 20 MeV) and ions (18 keV $\leq E_i \leq$ 150 MeV) in several energy intervals with good energy, species, time, and spatial resolution. (At Uranus the low- and high-energy cutoffs of the measurements were 22 keV and 1.2 MeV, respectively, for electrons and 28 keV and 3.5 MeV, respectively, for protons, due to the mode configuration.) Beyond an energy of $\sim$200 keV/nucleon (500 keV/nucleon at Uranus due to previous detector damage), individual ion species can be separately identified, and their energy spectra and angular distributions determined. Characteristics of channels relevant to this paper are listed in Table 1. Details of the LECP instrument have been presented in previous publications [*Krimigis et al.*, 1977, 1981; *Armstrong et al.*, 1981, 1983; *Hamilton et al.*, 1981] and will not be repeated here.

An important design feature of the instrument is its capability to obtain angular distributions, even though the spacecraft is three-axis stabilized. Angular measurements through 360° in a plane are made possible by the mounting of the detector telescopes on a rotating platform that is stepped through eight 45° cone sectors in periods ranging from 6 to 48 s per step, using a stepper motor. One of the eight angular fields of view is covered by a 2-mm aluminum shield (sector 8) to provide a background measurement for all detector channels in the conjugate sector (i.e., sector 4). The particular angular swath of the sky viewed by the instrument obviously depends on the

orientation of the Voyager spacecraft at any time. Details of the spacecraft orientation will be given later. At Uranus a special angular stepping mode was developed and was controlled by software in the main Voyager 2 computer. Because of the very rapid variations which were expected in *B-L* space, it was deemed desirable to perform the LECP stepping as rapidly as possible. However, owing to some interference with other Voyager 2 measurement programs, it was decided that the LECP would obtain rapid "snapshots" of the angular distributions every 12.0 min. Six-second sector stepping was used for these snapshots, and two complete angular scans were performed, lasting a total time period of 96 s. This special mode began at $\sim$0420 UT on day 24, 1986 (prior to the first bow shock crossing), and ended at $\sim$1500 UT on day 25, 1986 (well within the Uranian magnetotail). Outside this interval, continuous 48-s stepping was used (6.4 min per angular scan).

This paper constitutes the lead report of a series of articles on LECP results generated for this special issue. A follow-on paper by S. M. Krimigis et al. (Observations of energetic proton and electron enhancements upstream and downstream of Uranus' bow shock by the Voyager 2 spacecraft, submitted to *Planetary and Space Science*, 1987) (hereinafter S. M. Krimigis et al., submitted manuscript, 1987) will discuss upstream and downstream particle events observed near Uranus. Satellite-particle interactions, with emphasis on radiation effects on the satellites, are discussed by *Lanzerotti et al.* [this issue]. *Cheng et al.* [this issue] discuss particle phase space densities, and *Cheng* [this issue] calculates the expected heavy ion concentrations based on satellite-magnetosphere interactions.

VOYAGER 2 TRAJECTORY AND ORIENTATION

Within a frame of reference fixed to Uranus, the Voyager 2 spacecraft approached the Uranian system approximately within the solar ecliptic plane at a Uranian local time position of about 1300. The closest approach to the Uranian center (at $\sim$1758 UT on day 24 of 1986) was at $\sim$4.2 R_U (where 1 R_U = 25,600 km) on the duskside, and the spacecraft passed out of the Uranian system on the dawnside at a Uranian local time position of about 0220. The inbound bow shock and magnetopause positions occurred at distances of $\sim$24 and $\sim$18 R_U, respectively, from the planet center. The outbound magnetopause was encountered at $\sim$80 R_U, and numerous outbound bow shock crossings occurred at radial distances between $\sim$160 and 228 R_U [*Ness et al.*, 1986; *Bridge et al.*, 1986].

It is convenient for studies of magnetospheric configurations to present spacecraft trajectory information with respect to frames of reference fixed to the magnetic axis of the internal fields. Figure 1 shows such a presentation, where the horizontal axis ρ is the cylindrical radial distance from the axis of the magnetic dipole moment of Uranus (using the dipole moment orientation given by *Ness et al.* [1986]) and the vertical axis Z is the distance away from the dipole magnetic equatorial plane. Marked on the trajectory (in addition to time tick marks) are the positions where the spacecraft encountered the inbound bow shock (BS), the inbound and outbound magnetopauses (MP), and the four magnetotail neutral sheet (N1–N4) crossings as documented by *Ness et al.* [1986]. Also shown in the figure is the approximate position of the plane (labeled the [$\mathbf{R}_{S-U}$; $\mathbf{M} \times \mathbf{R}_{S-U}$] plane) along which one expects to find the neutral sheet of the very distant magnetotail (assuming that the sheet is untwisted [see *Ness et al.*, 1986]). The
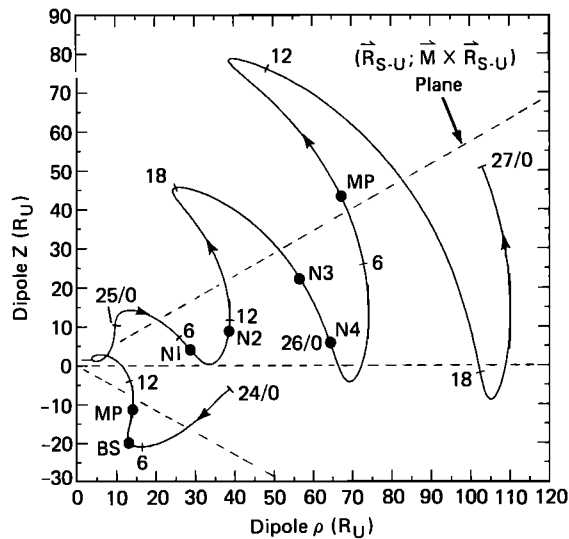
Fig. 1. Voyager 2 trajectory near Uranus expressed in the dipole magnetic cylindrical coordinate system using the offset tilted dipole model of Ness et al. [1986]. Rho (ρ) is the cylindrical radial distance between the spacecraft and the dipole axis line, and Z is the distance between the spacecraft and the dipole magnetic equator. The trajectory between day 24, 0000 UT, and day 27, 0000 UT, is shown. Marked on the trajectory are time ticks (every 6 hours) and the positions of the encounters with the inbound and outbound magnetopause (MP), the inbound bow shock (BS), and the four neutral sheet crossings (N1–N4) documented by Ness et al. [1986]. R_{S-U} is a vector lying along the Sun-Uranus line, and M is the magnetic dipole moment vector. The plane marked $[R_{S-U}; M \times R_{S-U}]$ is the average position of the plane along which one might expect the very distant (untwisted) neutral sheet to lie. With this coordinate system, that plane rocks by $\pm 7°$ from its displayed position according to the planetary spin phase.

position of this plane is only approximate because the spin axis of Uranus pointed about 7° from the Sun-Uranus line, causing the theoretical distant neutral sheet plane position to rock by $\pm 7°$ in angular position from its displayed position on the figure, depending on the spin phase of the planet. One might expect that at positions close to the planet the neutral sheet/plasma sheet structure would be positioned close to the magnetic equatorial plane (near $Z = 0$) while at distant positions this structure would approach (or would parallel) the distant neutral sheet plane. The neutral sheet crossings labeled N1, N2, and N3 appear to emulate that behavior. The crossing labeled N4 is anomalous, as will be discussed later.

Within the quasi-dipolar regions of the magnetic configuration it is convenient to present the trajectory of the spacecraft in a space which includes the L shell position. Of course, for a purely dipole configuration the L shell location is the radial distance to the magnetic equatorial crossing position of the field line on which the spacecraft is resident. The offset tilted dipole model presented by Ness et al. [1986] is used for the presentations given here. The reader should be aware, however, that more recent work by Connerney et al. [this issue] and M. H. Acuña et al. (Implications of Q3 Uranus magnetic field model for trapped particle motion, submitted to Journal of Geophysical Research, 1987, hereinafter referred to as submitted manuscript, 1987) has found that there are contributions to the magnetic configuration from higher-order terms in their multipole expansion. Comments will be made when appropriate; in those instances when it is crucial to have the most precise L shell positions, such as during our discussions of satellite absorption features, the latest model calculations

are used (calculations kindly supplied by M. Acuña and J. E. P. Connerney).

Figure 2 shows trajectory information for the spacecraft within the quasi-dipolar regions of the magnetosphere, calculated using the offset tilted dipole model. The bottom panel shows the logarithm of the L shell position versus the magnetic latitude, while the top panel shows the logarithm of L versus the logarithm of the model magnetc field strength (the model dipole moment is 0.23 gauss $R_U{}^3$). The B_0 line in the top panel is (for this purely dipolar model) the field strength that would be found by following the field line on which the spacecraft is resident to the magnetic equator (the minimum $|B|$ plane). One consequence of the higher-order multipole terms discussed in the previous paragraph is that the minimum $|B|$ plane becomes warped; in the bottom panel of Figure 2, between about 1800 and 2000 UT, the spacecraft apparently dips much more closely to the minimum $|B|$ plane than is indicated in the figure (M. H. Acuña et al., submitted manuscript, 1987). The vertical dashed lines in the bottom panel mark the minimum L shell positions of the five major Uranian satellites.

In order to accommodate observations by the Voyager scan platform instruments of the Uranian system, the rotational orientation of the spacecraft was changed at various times
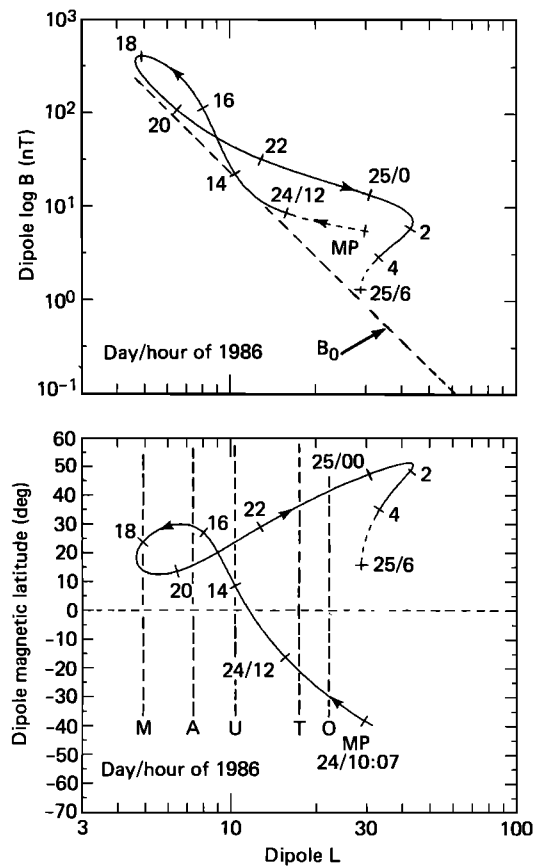

Fig. 2. Dipole L versus dipole magnetic latitude (bottom) and dipole L versus the dipole model field strength (top) for the Voyager 2 trajectory near Uranus, calculated using the offset tilted dipole model of Ness et al. [1986]. MP marks the magnetopause position. The time period between day 24, 1000 UT, and day 25, 0600 UT, is covered. In the top panel, B_0 is the field strength at the magnetic equator. In the bottom panel the vertical dashed lines mark the minimum L shell positions of the five major Uranian satellites.
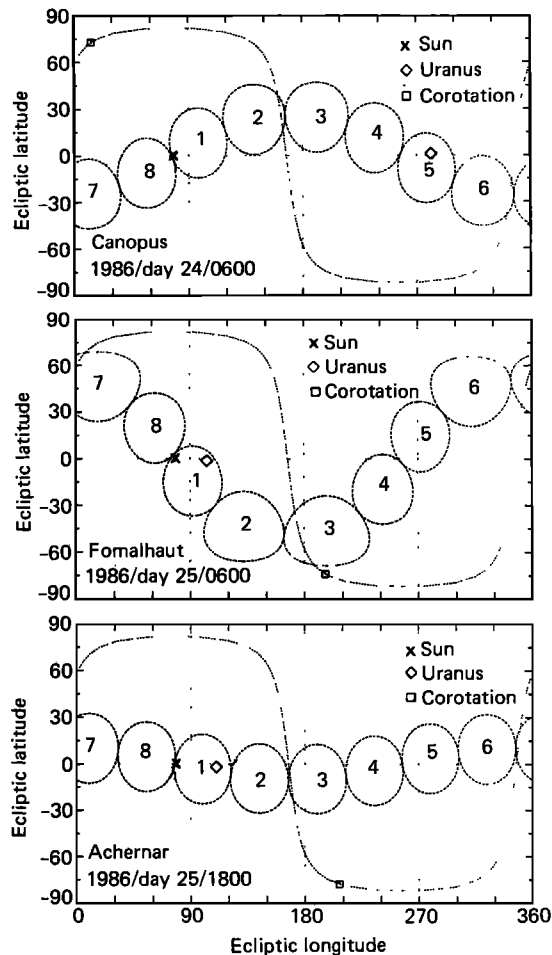
Fig. 3. Fields of view of the eight LECP view cones projected onto the solar ecliptic, 4π-steradian sky. The three panels correspond to different spacecraft roll orientation "star locks." Concerning ourselves only with the time period from day 24, 0000 UT, to day 27, 0000 UT, the "Canopus lock" was used from day 24, 0000 UT, to ~day 25, 0000 UT. The "Formalhaut lock" was then used until day 25, ~1230 UT. The "Achernar lock" was then used until day 26, ~1200 UT. Shown within the panels, in addition to the fields of view, are the directions to Uranus (appropriate only for the times listed in the panels), the directions to the Sun, the plane normal to the Uranus spin axis (the dotted line that weaves across the panel), and the direction of corotation within that plane.

throughout the magnetospheric encounter. These orientational changes strongly affected the measurement program of the LECP instrument, because angular distributions are measured only within a single plane. Typically, the spacecraft orientation changes involved simple rotations about the spacecraft-Earth line (or approximately the Sun-Uranus line). This line is approximately parallel to the LECP scan plane, and its projection passes almost exactly along the boundary between sectors 1 and 8 and sectors 4 and 5.

Figure 3 shows the regions of the 4π-steradian sky sampled by the eight 45° view cone sectors for three relevant roll orientations of the spacecraft. The axes of the panels are the solar ecliptic longitude and latitude. The positions of the Sun and of Uranus are indicated with the cross and open diamond (the positionings of the symbols are only accurate for the times indicated in the panels). Also shown, using the curved dotted line that weaves across each panel, is the plane that is normal to the Uranus spin axis. The corotation flow vector, uncorrected for the spacecraft motions and indicated by the open

square, lies within this plane. The top panel, corresponding to the "Canopus" star sensor lock position, represents the roll orientation of the spacecraft for most of the interval from about 54 hours prior to closest approach (CA at 1758 UT on day 24 of 1986) to about 6 hours after closest approach, with the exception of special maneuvers discussed below. The second panel, corresponding to the "Fomalhaut" star lock position, represents the roll position for about the first half of the observed magnetotail activity (from about day 25, 0010, to about day 25, 1230). The bottom panel shows the "Achernar" star lock roll position, used for the second half of the observed magnetotail activity (used from about day 25, 1230, until about day 26, 1200).

In many magnetospheric regions one is most concerned with the scan plane orientation with respect to the local magnetic field lines; Figure 4 shows the pitch angles of the particles measured by the eight LECP sectors for most of the quasi-dipolar regions of the magnetosphere (the lines correspond to the centers of the 45° view cones). The offset tilted dipole magnetic field model of Ness et al. [1986] was used to generate this figure. This display is particularly sensitive to special roll maneuvers of the spacecraft and is useful for determining whether events that appear within the flux profiles are simply the result of such maneuvers.

As described above, a special scan cyclic was used for much of the magnetospheric encounter, whereby complete angular scans were obtained only every 12.0 min. Most of the time the detectors were stationary within the sector 7 position. Sector 7 has been highlighted with the heavy line in Figure 4. Sector 8, which is the sector covered with a background shield, is represented in Figure 4 with the dashed line.

OVERVIEW OF THE URANIAN MAGNETOSPHERE

Plate 1 shows an overview of the LECP data (background subtracted) for the 3-day period covered by this paper. The top panel shows an energy-time differential intensity spectrogram of proton data for the energy range of 28–3500 keV (energies corresponding to the H^+ response of the detectors; we assume that all ions are protons, as shown by composition measurements at higher energies [Krimigis et al., 1986]). The white vertical bar between 1800 and 1900 UT on day 24 is used to mask regions of the proton spectra where intensities cannot be determined because of contamination by very ener-
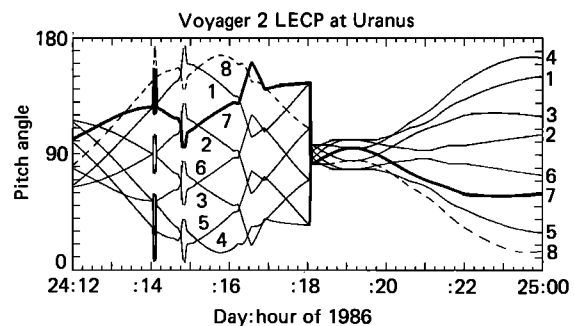

Fig. 4. Pitch angles of particles measured by the eight LECP view cones within the "core" magnetospheric regions at Uranus. The lines correspond to the centers of the 45° view cones. The pitch angles were calculated using the offset tilted dipole model of Ness et al. [1986]. Sector 7, the sector favored by the special scan cyclic mode, is highlighted with a heavy line. Sector 8, the background shielded sector, is shown with a dashed line. The Canopus star lock is used predominantly throughout, but special roll maneuvers were sporadically performed and are very apparent on the figure.
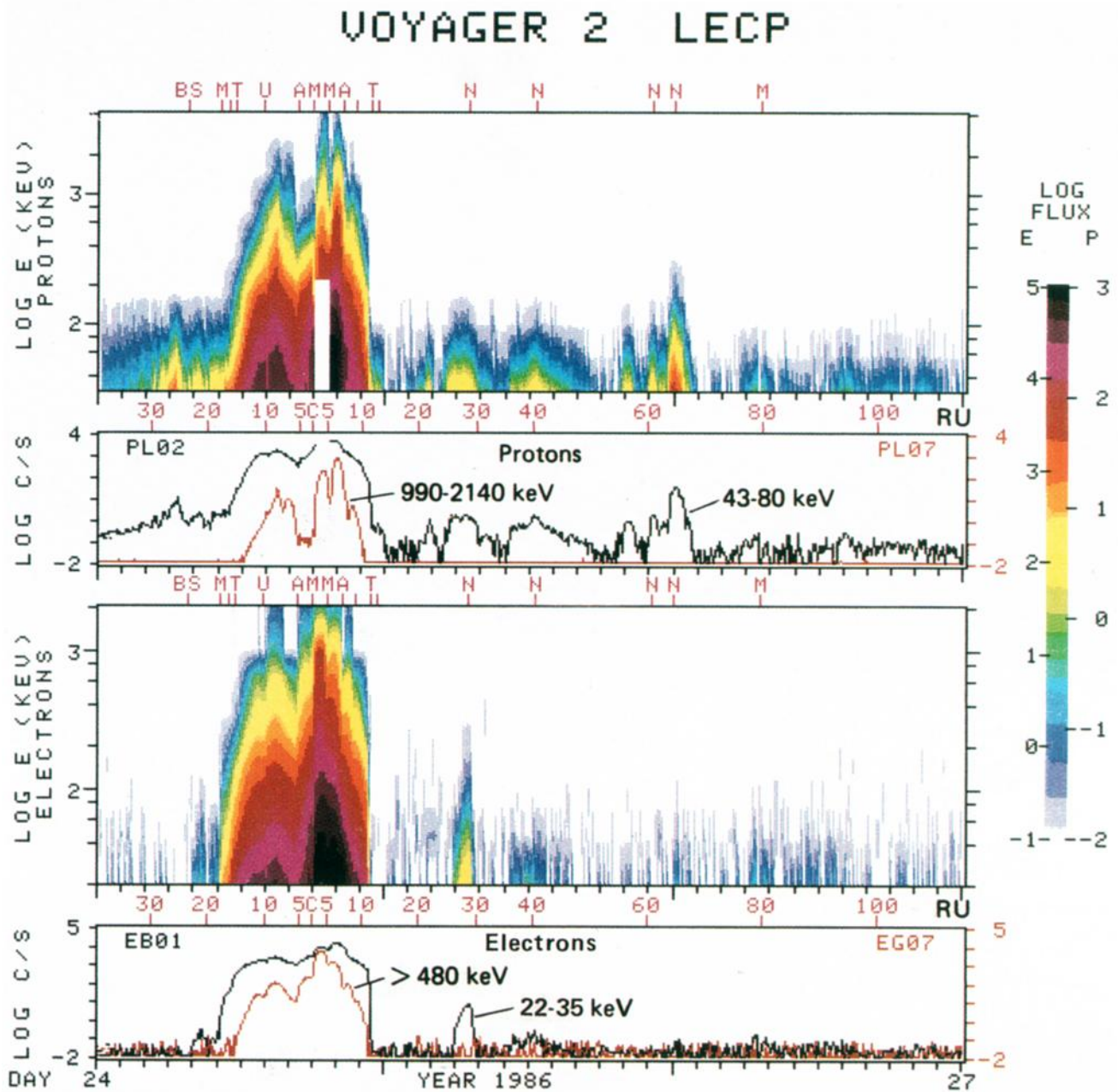
Plate 1. Color spectrogram overviews of a 3-day period that encompasses the Uranian magnetospheric encounter. The top panel shows an energy-time-intensity spectrogram of proton data for the energies 28 keV to 3500 keV. The color coding is according to the logarithm of the differential intensity (protons/cm^2 s sr keV) and is quantified with the color bar to the right of the figure (see the tick marks labeled "P"). The second panel shows count rate profiles for two selected proton channels: the 43- to 80-keV channel in black and the 990- to 2140-keV channel in orange. The third panel shows the energy-time-intensity spectrogram of electron data for the energies 22 keV to 1200 keV (use the "E" tick marks on the color bar). Finally, the bottom panel shows count rate profiles for two selected electron channels: the 22- to 35-keV channel in black and the >480-keV channel in orange (our high-energy differential channels are formed by taking differences between adjacent integral channels). Radial distances (plus the closest approach position C at $r = 4.2$ R_U) are marked above the second and fourth panels. Various events are marked above the first and third panels. The events are the bow shock (BS), the magnetopause (first and last M), the four neutral sheet crossings (N), and the inbound and outbound crossing times of the minimum L shell positions of the five major Uranian satellites (O, T, U, A, and M; the tick marks corresponding to O and to the second U are unlabeled because of space constraints).

getic electrons (electrons with $\gtrsim 400$ keV are not fully deflected by the sweeping magnet [see *Krimigis et al.*, 1977]). Fortunately, the LECP instrument measures the fluxes of electrons with $E \gtrsim 400$ keV, so we have good information on the degree of contamination. The second panel in Plate 1 shows the count rate profiles of two of the channels that were included in the construction of the proton spectrogram; the 43- to 80-keV channel, represented by a black line, and the 990- to 2140-keV channel, represented by an orange line. The third panel shows a spectrogram of the electron data from 22 to 1200 keV; the electron rate channels plotted in the bottom panel correspond to the energy ranges 22–35 keV (in black) and >480 keV (in orange). Radial distance markings are given just above the second and fourth panels (including the closest approach position C at $r = 4.2$ R_U); various encounter events are marked just above the first and third panels. The marked events are the bow shock crossing position (BS), the magnetopause crossing positions (first and last M), the times of the crossings of the minimum L shell positions of the five major Uranian satellites (Oberon, Titania, Umbriel, Ariel, and Miranda; where the tick marks corresponding to the Oberon L shell crossings and the second Umbriel crossing are unlabeled because of space constraints), and the times of the four magnetotail neutral sheet crossings (N) as documented by *Ness et al.* [1986].

The features displayed in Plate 1 will be the focus of detailed discussions in the sections that follow. Here we simply note some of the more general findings so that they can be viewed within the context of the entire magnetospheric encounter. A similar discussion for a portion of the data displayed was given by *Krimigis et al.* [1986], but that portion is repeated here for clarity.

Encountered first by the spacecraft within the displayed time period are intense upstream proton events with a peak intensity occurring about 27 R_U from the planet, just preceding the bow shock encountered near 24 R_U. The proton fluxes are low in the vicinity of the bow shock; however, the proton flux activity again picks up within the magnetosheath regions between the bow shock and the magnetopause. Of perhaps greater significance are the enhanced electron fluxes within the magnetosheath, with fluxes substantially higher than those observed preceding the bow shock crossing.

The magnetopause certainly marks the position where the more energetic fluxes begin to rise, but by comparison with other encountered magnetospheres (e.g., Jupiter and Saturn) this magnetopause appears relatively undistinguished [see *Krimigis et al.*, 1983, 1981]. This appearance could be a consequence of the relatively high entrance in magnetic latitude (Figure 1), as will be discussed. Inside the hard radiation region of the magnetosphere the more energetic proton and electron channels show minima or inflections associated approximately with the calculated minimum L shell positions of some of the satellites (see *Krimigis et al.* [1986] for a higher time resolution spectrogram of this region). Strong features are clearly associated with Umbriel, Ariel, and Miranda, and as described by *Krimigis et al.* [1986], more subtle features occur in association with Titania and perhaps Oberon. The lower-energy proton and electron channels do not show the substantial structure associated with the satellites that is seen in the higher-energy channels. Radial transport processes are apparently more efficient at these lower energies.

A very striking feature associated with the hard radiation zones is the sharp intensity decrease that occurred near 2240 UT on day 24. This cutoff could have been associated with the relatively close proximity of the minimum L shell position of

Titania and/or Oberon, or it could have been associated with a fortuitous coalescence of the instantaneous L shell positions of these two satellites at the spacecraft's L shell position at the time of the drop-off (as is suggested by *Ness et al.* [1986]). However, day-night magnetic drift asymmetries, coupled with magnetopause absorption on the dayside, offer a more likely explanation [see *Armstrong and Krimigis*, 1968]. The low-energy population that immediately followed the hard radiation cutoff indicates that the field lines remained closed.

The next principal features of interest are the numerous "plasma sheet" encounters which occurred predominantly during day 25. Plasma sheet protons are observed during each of the magnetic field neutral sheet crossings (marked on the top of the first and third panels). However, the proton enhancements are found to be not necessarily symmetric with respect to those crossings, and there existed substantial proton activity that was not associated in time with the neutral sheet encounters. Note in particular the curious low-energy ion component, mentioned above, observed for $\gtrsim 1$ hour immediately following, and abutted to, the sharp drop-off in the hard radiation ions near 2240 UT on day 24. This feature was observed at high latitudes within a region of quasi-dipolar field lines (well away from the regions where a neutral sheet might form). We will interpret this feature as corresponding to the so-called "horns" of the plasma sheet population. Electron enhancements are clearly associated with the first two neutral sheet encounters, and there may have been some activity associated with the other crossings as well.

Other features that will be discussed later are the proton and electron enhancements observed during the outbound magnetopause crossing, and an additional proton enhancement observed at ~ 1400 UT on day 26 within the outbound magnetosheath.

UPSTREAM AND INBOUND BOUNDARY REGIONS

Figure 5 shows further details of the upstream, magnetospheric boundary, and core magnetospheric regions. The top panel of the figure shows count rate profiles of the lowest-energy proton and electron channels. The structure within the upstream and magnetospheric boundary regions, the focus of the present section, can again be seen but with somewhat greater clarity. The second panel of Figure 5 shows information obtained using the angular scanning mode of the LECP instrument. Shown are the magnitudes and directions of the first-order angular anisotropies within the lowest-energy proton channel. The count rates as a function of look angle are fit to a harmonic function (i.e., $a_1 \cos (\phi - \phi_1)$), and the lengths of the "whisker" vectors shown in the figure correspond to the magnitudes of a_1, while the directions of the vectors correspond to the values of ϕ_1. Just to the left and right of the whisker panel are shown the relative directions to the Sun and to Uranus, given the roll orientation of the spacecraft, for the preencounter and postencounter time periods (the top panel of Figure 3 shows the corresponding sector sampling).

To fully explore the information contained in the anisotropies, it is necessary to describe the principal effects contributing to first-order anisotropies. There are two most common causes for the occurrence of first-order anisotropies: (1) bulk streaming of the distribution, in which case the direction of the corresponding whisker is the direction of "flow," and (2) nonzero Larmor radius sensing of spatial gradients in the particle pressure distributions, in which case the whiskers point parallel to the planes of constant pressure and tend to

point perpendicular to the magnetic field **B**. If the distribution function is isotropic in the center of momentum frame, then the first-order anisotropies can be represented mathematically with the equation [e.g., *Northrop et al.*, 1979]

$$A_1 = \rho \hat{b} \times \frac{\nabla f}{f} + \frac{1}{f}\frac{\partial f}{\partial v} V_c \qquad (1)$$

where ρ is the particle gyroradius, V_c is the velocity of the zero-momentum frame relative to the observation frame of reference, $\hat{b}$ is a unit vector along the magnetic field **B**, and $f = f(\mathbf{r}, \mathbf{v})$ is the distribution function. The first term in (1) represents the gradient anisotropy, and the second term represents the "flow" anisotropy. For a differential power law spectrum $(dJ/dE \sim E^{-\gamma})$, (1) can be rewritten in the form

$$A_1 = \rho \hat{b} \times \frac{\nabla f}{f} + 2(\gamma + 1)\frac{V_c}{v} \qquad (2)$$

Equation (2) is presented here only for qualitative discussions. For instance, it is evident from (2) that the first term increases with increasing energy while the second term decreases with increasing energy as $(E)^{-1/2}$.

For a disturbed region the anisotropies will often result from a combination of the two effects described above, requiring a very detailed analysis in order to unravel them [e.g., *Carbary et al.*, 1981; *Mitchell et al.*, 1986]. Such an analysis of complex regions is beyond the scope of the present paper. There are regions, however, where the interpretation of the anisotropies is relatively unambiguous. Figure 6 shows samples of the full LECP anisotropies from such regions for specific time periods shown in Figure 5 (indicated with tick marks and labels A–E below the whisker panel). The so-called "pie plots" shown give a representation of the angular scan plane of the detectors, with the radial extent of each pie section proportional to the normalized count rate detected within the corresponding sector. The count rate within the peak sector is marked on each pie plot. The nominal direction of the Sun and of Uranus is shown to the left of the second row of pie plots. The left-hand column of plots shows the anisotropies within our lowest-energy proton channel (28–43 keV), and the second column shows anisotropies within the next lowest channel (43–80 keV). The background sector 8 (the sector aligned with the scale) has been filled in by using a biharmonic fit to the other seven sectors (allowing for both first- and second-order anisotropies; see *Carbary et al.* [1981] for more details).

One key way of distinguishing between anisotropies caused by streaming or by pressure gradients is by noting the energy dependence of the degree of anisotropy. As noted in our discussion of equation (2), in the event that the distributions are not substantially anisotropic within the zero-momentum frame of reference, one expects that the anisotropies will be most substantial in the lowest-energy channels for a streaming situation and most substantial in the highest-energy channels for a spatial gradient situation (assuming in each case a reasonable energy distribution). The top two rows and the bottom row of pie plots in Figure 6 (rows A, B, and E) show what appear to be streaming situations, while the third and fourth rows (rows C and D) show what appear to be gradient anisotropies.

The orientation of the anisotropies with respect to the magnetic field direction can supply additional evidence for the interpretation of the anisotropies. For rows A and B the projection of the magnetic direction onto the scan planes is
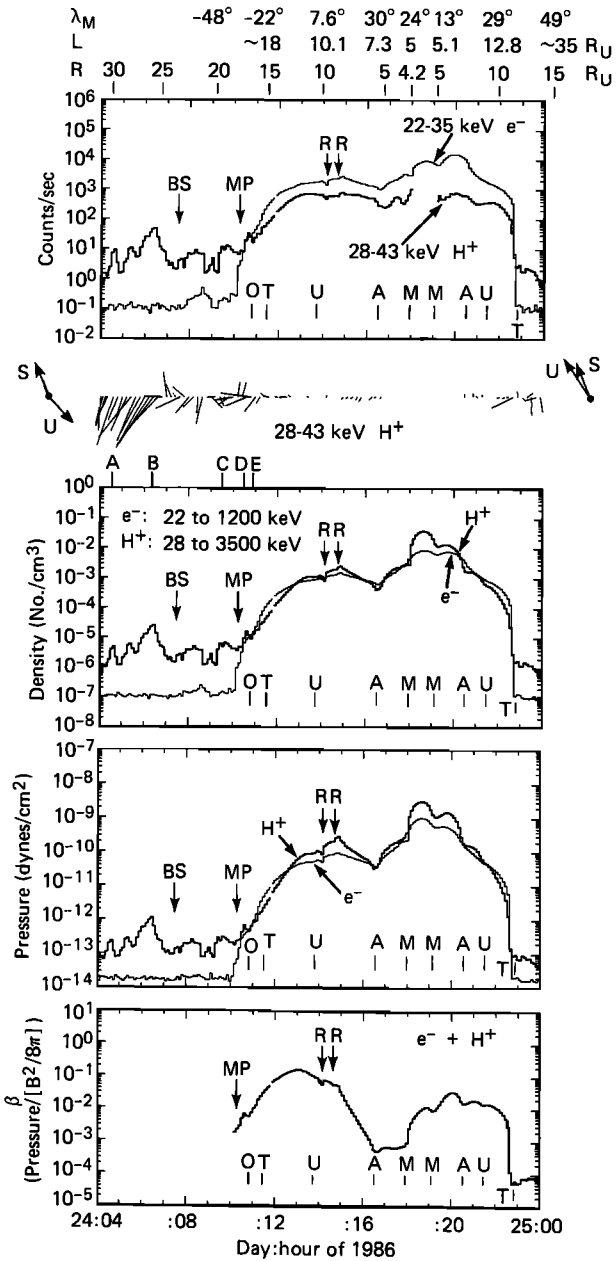

Fig. 5. The five panels show (from top to bottom) count rates of the lowest-energy LECP proton and electron channels: anisotropy "whisker" vectors showing the magnitude (length) and direction of the first-order anisotropies of the lowest-energy proton channel (the preencounter and postencounter directions to the Sun and to Uranus are shown to the left and right, respectively); the integrated proton and electron number densities; the integrated proton and electron pressures; and the ion plus electron plasma β parameter (ratio of particle pressure/magnetic pressure) calculated using the offset tilted dipole model of *Ness et al.* [1986]. The crossing times of the minimum L shell positions of the five major satellites (O, T, U, A, M) are shown at the bottom of four of the five panels. BS, MP, and R correspond to bow shock, magnetopause, and spacecraft roll, respectively. Radial position, L shell position (information provided by M. H. Acuña calculated using the lastest multipole expansion magnetic field model [*Connerney et al.*, this issue; M. H. Acuña et al., submitted manuscript, 1987]), and dipole magnetic latitude are shown above the top panel. The five tick marks labeled A, B, C, D, and E above the third panel are the sampling times used for Figure 6.

shown, and the streaming appears to be in the general direction of **B**. However, the component of **B** out of the LECP scan plane (pointing down into the page) is comparable to the component within that plane. Hence the possibility that convective
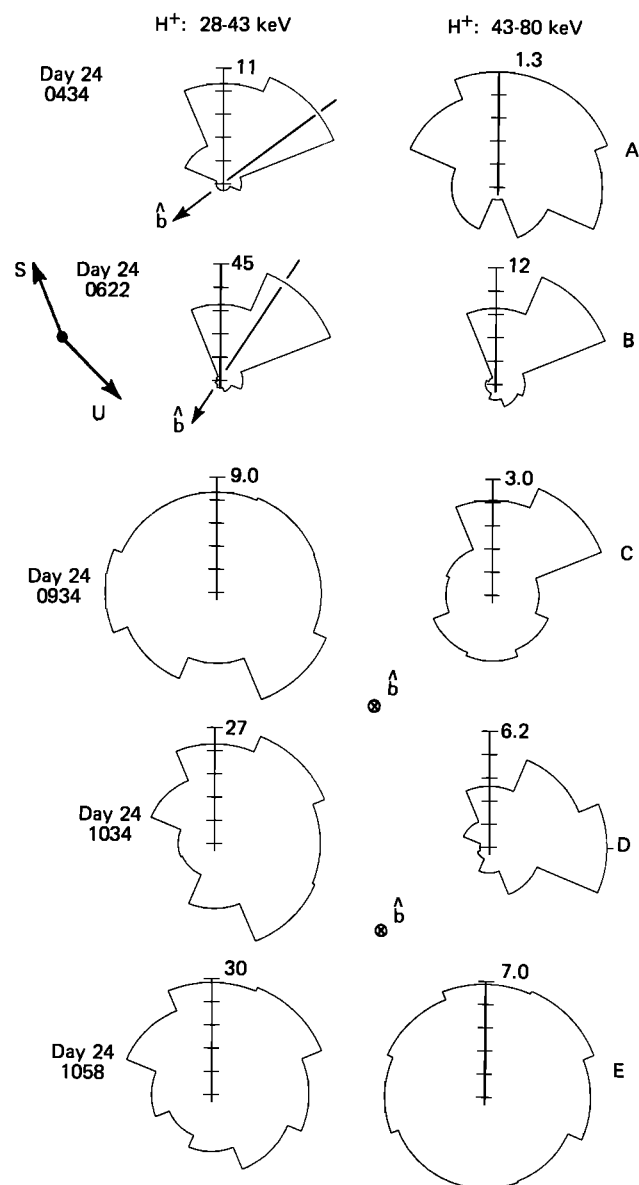
Fig. 6. Angular anisotropy "pie plots" sampled from the five different time periods (rows A–E) shown with labeled tick marks above the third panel in Figure 5. The radial extents of the pie sections are proportional to the normalized intensities observed within the eight LECP angular sectors. The left-hand column corresponds to our 28- to 43-keV proton channel, and the right-hand column corresponds to our 43- to 80-keV proton channel. The directions toward the Sun and toward Uranus are shown to the left of row B. The background shielded sector 8 (pointing straight up) has been filled in with a biharmonic fit to the other seven sectors. The projection of the magnetic field direction $\hat{b}$ onto the LECP scan plane is shown in the left column of rows A and B. The field points predominantly perpendicular to the scan plane (and into the page) for the other rows.

flows (flows perpendicular to **B**) or that spatial gradients contribute to the anisotropies cannot be eliminated. For the other three rows of plots in Figure 6, the field **B** points predominantly perpendicular to the scan plane, so that the interpretation must be based largely on the energy dependence of the anisotropies.

Returning now to the top two panels of Figure 5, we observe (from the top two rows of Figure 6 and from the context of the observations) that the ions observed upstream of the

bow shock were streaming very rapidly toward the duskside of the magnetosphere and approximately normal to the direction of Uranus (i.e., tangentially to the average magnetospheric boundaries). Given the position of the spacecraft (at ~ 1300 local time), it would appear that these ions were being generated (e.g., escaping from the magnetosphere (S. M. Krimigis et al., submitted manuscript, 1987)) in the vicinity of the nose of the magnetosphere.

There is an additional possibility. The upstream ions observed in Figure 5 are qualitatively very distinct from the interplanetary events observed earlier and later [see *Krimigis et al.*, 1986, also submitted manuscript, 1987]. Not only are the intensities 1–2 orders of magnitude greater for the Figure 5 events, but the flow signature is also somewhat peculiar in being nearly tangential to the magnetospheric surfaces. Such signatures are more commonly observed within the magnetosheath regions (for example, see *Krimigis et al.* [1979] for the characteristics at Jupiter). We suggest the possibility that the observed upstream ions in Figure 5 are the leftover remains of magnetosheath populations after the bow shock has moved planetward. There is some evidence from the plasma waves experiment (PWS; W. S. Kurth, private communication, 1987) that prior to the bow shock encounter the bow shock was further out than it was at its encountered position. In particular, plasma oscillations, sometimes associated with a "close" bow shock proximity, were observed as early as 0315 UT on day 24 (see Figure 3 of *Gurnett et al.* [1986] for a plot beginning at 0400 UT). These observations are suggestive that the bow shock could have "enclosed" the observed ions just prior to their detection. However, detailed comparisons will have to be performed with the Voyager magnetic field data (MAG) to eliminate the possibility that the plasma oscillations resulted from peculiar spacecraft/bow shock magnetic connection geometries.

Rows C and D in Figure 6 were taken from positions just outside and inside the magnetopause regions in Figure 5. Given the direction of **B**, the directions of the anisotropies reveal the expected pressure gradient pointing in the general direction of the planet. Row E in Figure 6 was sampled well inside the magnetopause and appears to represent a convective boundary layer flow flowing tangentially to the average magnetopause surface. Approximate Compton-Getting calculations [e.g., *Roelof et al.*, 1976] yield a flow velocity of >200 km/s.

The interpretation of the other anisotropies represented in Figure 5 must await more detailed studies that will follow. It is clear, however, that while the bow shock and magnetopause may look relatively conventional on a flux-time profile, they are rather revealing with respect to the anisotropies. In particular, if the highly variable whiskers in the vicinity of the magnetopause represent spatial gradients, the surface of the magnetopause must be extremely dynamic, with normal vectors pointing at times in what appear to be random directions. If bulk streaming has a role to play, then LECP could have measured the types of cross-magnetospheric transport processes that have been attributed to the Earth's magnetopause regions (particle leakage, possible reconnection processes, impulsive penetration, etc.).

We will return to Figure 5 later in order to discuss the moments of the particle distributions shown there for the hard radiation or "core" magnetospheric regions. There is one item concerning such moments that is relevant to the present section, however. The second from the bottom panel of Figure 5 shows the total integrated pressures (two thirds of the energy density) of the ions and electrons that existed within the

LECP range of energies. Within the upstream proton regions the proton pressures peaked at $\sim 3 \times 10^{-13}$ dyn/cm^2 (the value shown in Figure 5 is high, because most of the sampling came from sector 7—recall our special scan cyclic—and because sector 7 faced the "ram" direction of the streaming ions). This value of proton pressure was substantially larger than was the corresponding magnetic pressure ($B^2/8\pi$: 4×10^{-14} dyn/cm^2) calculated using Figure 1 of *Ness et al.* [1986]. However, from solar wind parameters given by *Bridge et al.* [1986] for the preshock conditions, the solar wind pressure within the zero-momentum frame of reference ($\sim 4 \times 10^{-12}$ dyn/cm^2) was an order of magnitude higher than that contained within the observed upstream ions. Given that there may have been substantial upstream proton pressure content within the energy range below the sampled range (note that $j \propto E^{-4}$), the solar wind pressures may not have overwhelmed the upstream proton pressures, and such upstream ions could have introduced some perturbation to the medium, as is often the case in the upstream region of all other planets (S. M. Krimigis et al., submitted manuscript, 1987). The upstream proton pressures would have matched the solar wind pressures if the proton power law spectral shape continued down to 10 keV from the 28-keV LECP lower limit.

SATELLITE AND OTHER SIGNATURES WITHIN THE "CORE" MAGNETOSPHERE

As was discussed extensively by *Krimigis et al.* [1986] and *Stone et al.* [1986], the satellites of Uranus have a substantial influence on the more energetic trapped particle populations. Using the offset tilted dipole model of *Ness et al.* [1986], it was shown by *Krimigis et al.* [1986] and *Stone et al.* [1986] that the observed "flux minima" were somewhat aligned with the minimum L shell positions of the satellites (i.e., $L_{\min}$ is approximately the satellite radial position at the magnetic equator). This finding fits one's intuition (a satellite spends most of its time at its minimum and maximum L shell positions) and is predicted by detailed modeling of time-averaged particle lifetimes against particle absorption by the satellites within the Uranian system [*Paonessa and Cheng*, 1987]. However, the matching of the minimum L shell positions with the absorption features was by no means quantitatively exact. Satellite signatures provide important information about particle transport processes. In order to extract such information it is important that the absence of coincidence between the predicted and observed signatures be resolved. Such disagreements can be a reflection of the degree of accuracy of the field model or of the fundamental understanding about how the trapped particles interact with the satellites.

Using the spacecraft L versus time information calculated using the latest multipole expansion model of Uranus' magnetic field configuration (courtesy of M. H. Acuña and J. E. P. Connerney [see *Connerney et al.*, this issue; M. H. Acuña et al., submitted manuscript, 1987], Figure 7 shows the count rate versus spacecraft L for four different LECP channels (using only the sector 7 data). From top to bottom the plots show high-energy electrons, high-energy ions, low-energy electrons, and low-energy ions. In the top two profiles the outbound rates have been raised by 2 orders of magnitude with respect to the inbound rates for purposes of clarity. In the bottom two profiles a discontinuity in the inbound portions near $L \approx 16.5$ (labeled "D") corresponds to a switch from the offset tilted dipole calculation of the L shell positions to the multipole expansion calculation of L shell positions as the spacecraft moves planetward (the calculations supplied to us
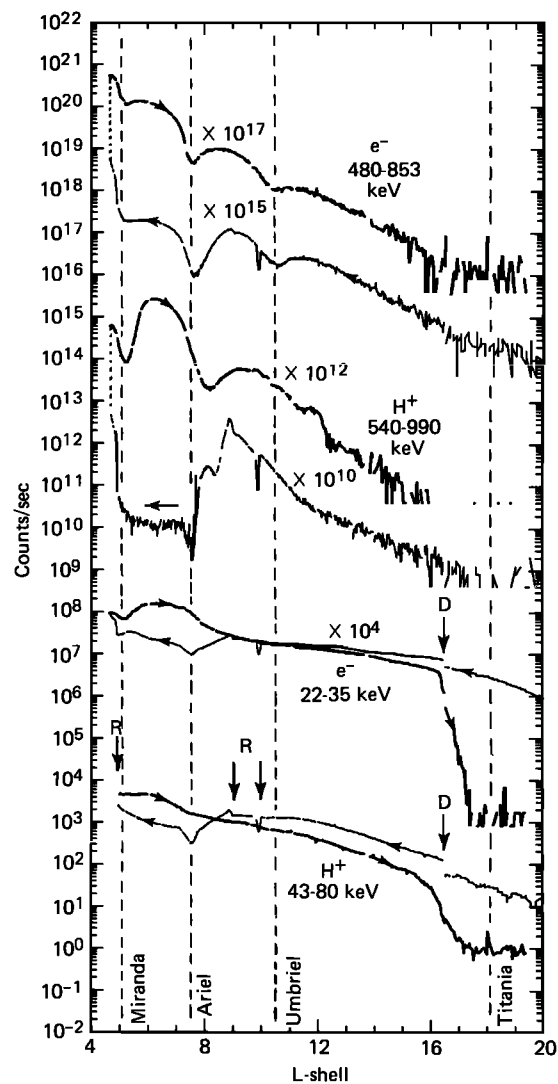

Fig. 7. Count rate versus spacecraft L shell position for four of the (sector 7) LECP rate channels. The L shell positions, kindly provided by M. H. Acuña and J. E. P. Connerney, were calculated using the latest multipole expansion magnetic field model of *Connerney et al.* [this issue] and M. H. Acuña et al. (submitted manuscript, 1987). The data to the right of the discontinuity labeled "D" for the inbound data only were plotted versus the offset tilted dipole L shell positions [*Ness et al.*, 1986]. The arrows labeled "R" indicate positions of sudden roll reorientations of the spacecraft for the inbound data. Slower roll maneuvers occurred elsewhere. The vertical lines correspond to the average minimum L shell positions of the four innermost major satellites.

did not extend to earlier times). The $L > 16.5$ regions are included to demonstrate that the sharp drop-off that occurs near but beyond $L = 16$ on the outbound leg is not reflected in the inbound leg profile. The vertical dashed lines correspond to the "average" minimum L shell positions of the four inner satellites. It is noted by M. H. Acuña et al. (submitted manuscript, 1987) that because of asymmetries in the planet's internal magnetic configuration the minimum L shell position depends on the satellite's orbital history versus the planetary spin phase history ($\Delta L_{\min} \sim 0.25$).

Considering first the top profile of Figure 7 (high-energy electrons), it is clear that the flux minima, while not exactly ordered, are reasonably well ordered by the latest field model. Comparisons with Figure 3 of *Krimigis et al.* [1986] show that

the new magnetic field model improves the inbound/outbound alignment of the flux minima over that obtained with the offset tilted dipole model. Additionally, the minima are reasonably well aligned with the average satellite minimum L shell positions.

The spatial behavior of the energetic ions is substantially more complex than that of the electrons. Most peculiar is the behavior in the vicinity of Ariel. On the outbound profile the flux minimum is not nearly as aligned with the minimum Ariel L shell as are the electron minima. On the inbound profile there appear to be two features, one at $L \approx 8.3$ and another at $L \approx 7.7$. (As is revealed by Figure 4, the feature near $L \approx 7.7$, corresponding to ~ 1635 UT, occurred during a spacecraft orientation maneuver, and the exact positioning there should be viewed with caution.) At the Umbriel minimum L position there appears to be very little disturbance in the energetic proton profile. The feature near $L \approx 11.3$ and beyond on the outbound leg could presumably be associated with Umbriel, or some other effect.

The energetic electron profile clearly provides some verification of the accuracy of the latest multipole magneitc field model [*Connerney et al.*, this issue; M. H. Acuña et al., submitted manuscript, 1987]. We suggest that the misalignments and structures within the energetic proton profile may be due to our limited understanding of how the flux inflections are created. In particular, some of the details of the features may be due to a sensitivity to the instantaneous positions, as opposed to the time-averaged positions, of the satellites. However, as described later, time variations are at least partially responsible. In these later discussions we suggest that substorms are occurring within the Uranian magnetosphere, and it is suggested both in the present work and in the work by *Cheng et al.* [this issue] (based on LECP phase-space-density calculations) that substorms or similar kinds of time variations are responsible for generating and/or modifying some of the energetic proton features.

The lower-energy electron and proton channel profiles show far less satellite-associated structure than do the higher-energy channels. Some features are apparent, but the readers can make their own judgments (caution should be exercised concerning spacecraft roll maneuvers on the inbound leg in the vicinity of the Ariel minimum L shell, near 1630 UT, and just inside the Miranda L shell near 1800 UT). Presumably, there are radial transport processes that help smear spatial structures for the lower-energy particles. As noted earlier, the most striking feature within the lower-energy channels is the very sharp dropout outside $L \sim 16$ on the outbound leg. This feature does not coincide with the minimum L shell positions of Titania or Oberon (at $L \approx 22.8$). As mentioned earlier, this drop-off probably results from dayside magnetopause absorption coupled with day-night magnetic drift asymmetries [*Armstrong and Krimigis*, 1968].

There is one final feature in Figure 7, keynoted by *Krimigis et al.* [1986], that is of substantial interest. Between the minimum L shell positions of Miranda and Ariel the energetic proton rate profile exhibits a very substantial (>3 orders of magnitude) apparent inbound/outbound asymmetry. If this asymmetry were real and not just apparent, it would imply that the magnetosphere is much more dynamic then would otherwise be concluded. Figure 2 (bottom) shows that the spacecraft was closer to the magnetic equator during the outbound pass at the relevant L shell position ($L \sim 6.3$) than it was during the inbound pass. The top panel of Figure 2 shows that the difference in field strengths between the two positions
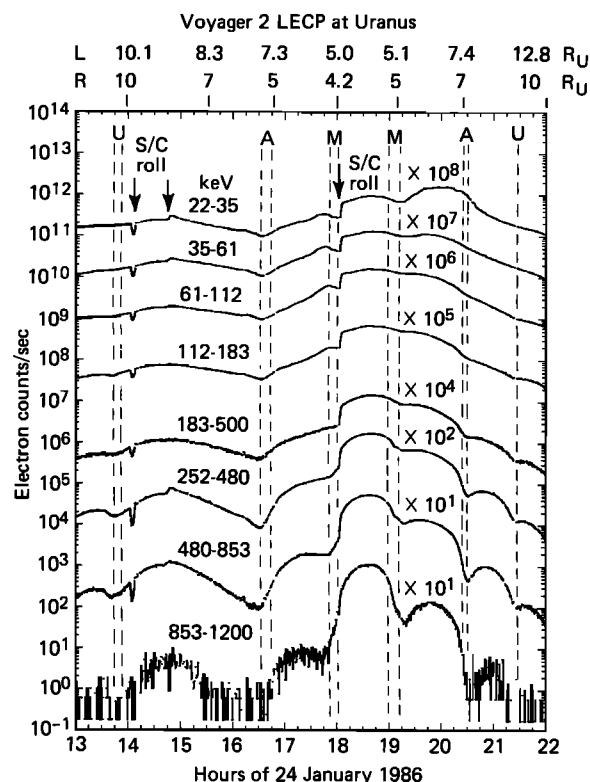

Fig. 8. Count rate versus time for the eight primary LECP electron channels within the inner magnetospheric regions. "Sudden" spacecraft roll maneuver positions are marked near the top. The double vertical dashed lines (two lines per Uranian satellite encounter) correspond to times when the spacecraft encountered the extremes of the variable minimum L shell positions of the three innermost major satellites (positioned using calculations kindly supplied by M. H. Acuña and J. E. P. Connerney). Radial spacecraft position and spacecraft L shell position (M. H. Acuña et al , submitted manuscript, 1987) are shown above the panel.

was of the order of a factor of 2. Since conservation of magnetic moment and energy require that $\sin(\alpha_2) = \sin(\alpha_1)(B_2/B_1)^{1/2}$, where α_1 and α_2 are the particle pitch angles of the particles at the two positions sampled, the inbound/outbound asymmetry would be eliminated if all of the substantially enhanced outbound fluxes were confined to pitch angles between $45°$ and $135°$ (obtained by setting α_2, the inbound value, equal to $90°$). We shall see in a later section that there is some evidence that this condition was met, suggesting that the dramatic inbound/outbound asymmetry was only apparent and not real.

Figures 8 and 9 show additional details of the flux profiles within the innermost regions of the magnetosphere, allowing for a higher-resolution comparison between predicted and observed satellite signatures. Figure 8 shows profiles of eight differential energy electron channels, from 22 keV to 1200 keV, and Figure 9 shows the equivalent for protons (28 keV to 3500 keV). The times of the crossings of the minimum L shell positions of the satellites are represented with two dashed lines per crossing. As noted earlier, the minimum L shell positions of the satellites depend somewhat on recent history (M. H. Acuña et al., submitted manuscript, 1987). The double dashed lines represent the extremes of that variability calculated since the beginning of day 23, 1986 (data kindly supplied by M. H. Acuña and J. E. P. Connerney).

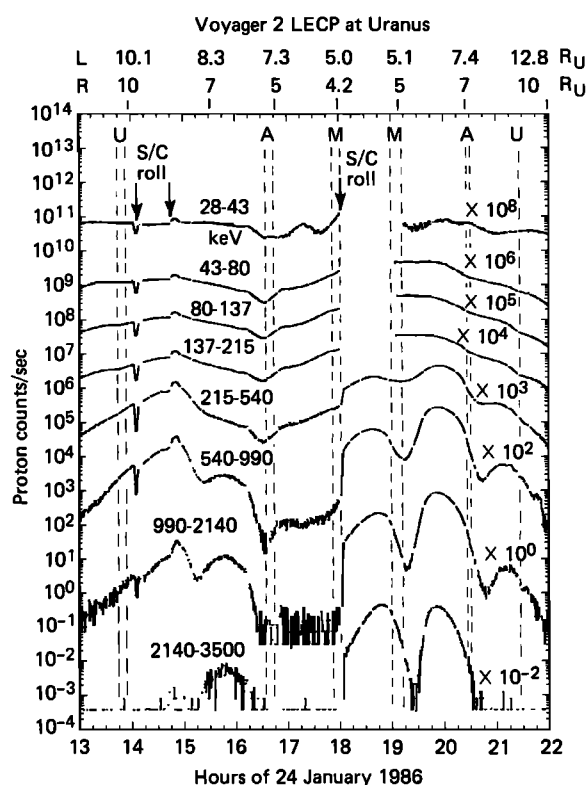One expects on the basis of the fully time-averaged models

Fig. 9. Same format as Figure 8, but for our eight primary proton channels, rather than for electrons.

[*Paonessa and Cheng*, 1987] that the minimum *L* shell positions will reside exactly within the flux minima features. Figure 8 shows that there are deviations away from this alignment in the higher-energy electron channels, particularly in the vicinity of Miranda (both inbound and outbound). Either the magnetic field model has some inaccuracies associated with it, or the time-stationary models of satellite absorption are not fully adequate. It is of interest that the flux minima outbound, in the vicinity of Miranda, and perhaps in the vicinity of Ariel as well, show two inflections in slope, one minor and one major, perhaps associated with the variability of the minimum *L* shell positions. Because of the roll maneuvers near Ariel and Miranda one must be cautious in interpreting the inbound features. The importance of source and loss mechanisms in addition to satellite sweeping is revealed by the electron phase space density profiles [*Cheng et al.*, this issue], which indicate injection of high-energy electrons between the satellite minimum *L* shells.

A most striking feature in Figure 9 is the enhancement centered at ∼1545 UT in the highest three proton energy channels. (There is a corresponding flux minimum near ∼1515 UT that we noted in our discussions of Figure 7 at *L* ∼ 8.3.) There are several conditions that make this enhancement feature unusual. First, it occurs during a flux minimum within the highest-energy electron channels (see Figure 8). Second, by using Figure 2 to determine when the corresponding feature might be expected to be observed on the outbound pass (∼2045 UT), one finds that there is no corresponding outbound feature. What is more, Figure 2 shows that the inbound observation position occurred at a higher magnetic latitude than did the outbound position. Thus the feature could not have been "hidden" from the spacecraft on its outbound leg. All of these characteristics give credence to the

suggestion (see also *Cheng et al.* [this issue]) that dynamical time variations (e.g., substorm injection effects) are modifying the energetic ion populations. For the purposes of later discussions, we will refer to this 1545 UT ion event as an "injection event."

A final feature of note in Figure 9 is the distinct bump in the lowest-energy proton channel, peaking near 1720 UT. This feature is not reflected in the higher-energy channels. The region encountered between 1700 and ∼1730 UT is just where the hot plasma (*kT* up to 1 keV) detected by the plasma science (PLS) detectors (<6-keV particles) maximized in intensity [*McNutt et al.*, 1987]. One possibility is that this bump in the lowest-energy channel results from the high-energy tail of this high-temperature (by PLS standards) plasma component. The density of the hot PLS component maximizes near 1730 UT; however, the temperature of the hottest component is somewhat lower at 1730 UT than it is at 1720 UT [*Selesnick and McNutt*, this issue]. Between 1800 and 1900 UT in Figure 9 the four lowest proton energy channels have been blanked out because of energetic electron contamination, as described earlier.

DISTRIBUTION MOMENTS AND THEIR IMPLICATIONS

We return to Figure 5, where the bottom three panels show moments and normalized moments of the LECP electron and proton distributions, with the electron moments represented by light lines and protons by heavy lines (when a distinction is being made). Our concern here will be with the hard radiation or core magnetospheric regions encountered between ∼1000 and ∼2300 UT. The lower portion of each plot shows the approximate times of the crossings of the minimum *L* shell positions of the Uranian satellites, as described in the last section. Satellite structure appears within the moments as well as in the flux profiles. Because of the electron contamination problem between 1800 and 1900 UT, the moments shown between these times for the ions should be considered lower limits for the moments corresponding to the measured LECP range of energies.

The third panel from the bottom shows proton and electron number densities. Typically (with the possible exception of Jupiter [see *Krimigis et al.*, 1981]), the number densities within the LECP range are small as compared to the densities within the PLS range of energies (10 eV to 6 keV). Our absolute peak density (for LECP ions) was 0.04 cm^{-3} (within the "lower limit" zone), which should be compared to the ∼0.25–2.5 cm^{-3} densities recorded by PLS at lower energies between 1700 and 1930 UT [*McNutt et al.*, 1987]. Outside this time period, the <6-keV densities continue to dominate over the LECP densities by an order of magnitude out to at least *L* ∼ 9 *R*$_U$ [*Selesnick and McNutt*, this issue].

The situation is different for the pressure calculations, since typically it is the particles within the LECP range of energies which have been found to dominate at other magnetospheres [*Krimigis et al.*, 1981, 1983; *McNutt*, 1984]. Calculations of electron and proton pressures from the LECP data are shown in the second from the bottom panel of Figure 5. Note that in many regions the electron pressures are comparable and indeed sometimes exceed the proton pressures.

With regard to magnetospheric configurations a most important plasma parameter is the ratio of the total particle pressure to the magnetic field pressure ($B^2/8\pi$). This "β" parameter is plotted in the bottom panel of Figure 5. The plot shows that the largest value of the parameter that was ob-

served was $\beta \sim 0.13$ at ~ 1300 UT close to the magnetic equator (Figure 2). This value is low as compared to the magnetospheres of Earth, Jupiter, and Saturn. Unlike the case of the magnetospheres of Jupiter and Saturn [see *Krimigis et al.*, 1981, 1983; *Lanzerotti et al.*, 1983; *Maclennan et al.*, 1983], the hot trapped populations at Uranus appear to play essentially no role in establishing the standoff position of the magnetopause. If that conclusion is valid, then the magnetosphere of Uranus more closely emulates classical models of a magnetospheric configuration than do the other visited magnetospheres [e.g., *Hess and Mead*, 1965]. We caution the reader, however, that the spacecraft entered the system at a relatively large magnetic latitude. As we will note later in our discussion of pitch angle distributions, conditions near the magnetic equator may have been very different from conditions at the entrance position.

Ring Current Shielding of the Convection Field

It was implied earlier in this section that it is likely that the pressures are dominated by the energetic particles measured by the LECP instrument. That statement may not be true for several specific magnetospheric regions. The issue has become of substantial importance with the realization that solar wind-driven convective transport may have an important role to play for the lower-energy (<6-keV PLS range) plasmas [*Selesnick and Richardson*, 1986; *Vasyliunas*, 1986]. The principal issue is the interpretation of the sharp cutoffs in the "hot" plasma component observed near 1730 UT inbound and near 1855 UT outbound [*Bridge et al.*, 1986; *McNutt et al.*, 1987]. The hot (PLS) plasma all but disappears inside the L shells corresponding to above stated times. These cutoffs have been interpreted by McNutt et al. and *Selesnick and McNutt* [this issue] as being generated by a dramatic shielding of the solar wind-generated convection electric field at the position of the cutoffs. The reason that the issue of predominance with regard to the pressure contributions is so important is that standard models of "region 2" field-aligned current generation, and of the corresponding charge separation that gives rise to the electric field shielding, depend on the presence of a particle pressure gradient that points radially away from the planet [e.g., *Block*, 1984]. LECP pressure profiles do not follow the behavior of the lower-energy particles. Thus if the LECP particles predominated in terms of particle pressure, then the electric field shielding model might have to be reconsidered.

With regard to the LECP pressures in the vicinity of the PLS plasma cutoffs, we must first recall the discussion given in the previous section concerning the apparent inbound/outbound asymmetry between the L shells of Ariel and Miranda. That region of the LECP asymmetry corresponds to the inbound region where the first PLS plasma cutoff was observed. It was concluded in the previous section (based partially on evidence to be presented in sections below) that the asymmetry was only apparent and not real. It is our belief that the LECP pressures at the equatorial position along the L shell encountered at ~ 1730 UT (the position of the first plasma drop-off) will equal the corresponding pressure seen at the same L shell along the outbound leg. That pressure ($e^- + H^+$) is about equal to $\sim 2 \times 10^{-9}$ dyn/cm^2 (with no extrapolations to lower energies) and corresponds to a plasma β value of 0.03. At the outbound PLS plasma dropout position (at ~ 1855 UT) we need no arguments concerning inbound/outbound asymmetries. The LECP pressure there was $\sim 3.6 \times 10^{-9}$ dyn/cm^2, corresponding to a plasma β value of ~ 0.01 (this value is a lower limit due to the blanking out of our

lowest four proton channels in this region). On the basis of the density and temperature profiles given by *Selesnick and McNutt* [this issue], it would appear that the LECP pressures are somewhat greater than the PLS values. Clearly, detailed comparisons will have to be performed before the viability of the *McNutt et al.* [1987] and *Selesnick and McNutt* [this issue] model of electric field shielding at Uranus can be established (in particular the scaling arguments concerning the boundary positions). There are other processes (as at Earth) that can generate plasma cutoffs, as will be discussed in the last section.

Whistler Mode Stably Trapped Flux Limit

The plasma β parameter calculations leave one with the impression that the Uranian magnetosphere is relatively empty. However, one is left with a different impression when the particle fluxes are examined. In particular, the energetic electron flux in the Uranian radiation belt is very high in the following sense: the integral electron flux substantially exceeds the whistler mode stably trapped limit (as first pointed out by E. C. Stone, private communication, 1986). The stably trapped flux limit is the flux of resonant electrons such that significant growth of unstable whistlers can occur during a single wave traversal of the unstable region along a field line [*Kennel and Petschek*, 1966]. If this limit is exceeded, intense whistler mode waves are excited, causing rapid pitch angle scattering and precipitation losses of electrons. Unless a sufficiently strong electron source is present, the excitation of unstable whistlers and consequent precipitation losses serve to regulate the resonant electron flux. The whistler mode stably trapped limit is conventionally cited as an upper limit to the radiation belt fluxes, and it is well known that at Earth the integral $\gtrsim 40$-keV electron flux lies generally near or below this limit [*Kennel and Petschek*, 1966]. However, this limit is exceeded in the inner magnetosphere of Uranus. We estimate the stably trapped limit at Uranus to be

$$J^* \approx \frac{B}{A_e - A_c} \frac{\ln G}{l} \frac{c}{2\pi^2 e} \approx 4.3 \times 10^9 L^{-4} \quad \text{cm}^{-2} \text{ s}^{-1} \quad (3)$$

where we have assumed an anisotropy factor $A_e - A_c = 0.2$, a gain factor $\ln G = 3$, and an interaction length $l = LR_U$. These factors are the conventional ones used for the Earth's magnetosphere [e.g., *Kennel and Petschek*, 1966]. The factor $A_e - A_c$ gives rise to the greatest uncertainty. However, as will be shown later, the observed pitch angle distributions have well-developed pancake shapes throughout the magnetosphere. Hence our calculated J^* is most likely an upper limit.

The measured differential electron intensity near Uranus $L = 4.73$ was (from panel G of Figure 10, *Krimigis et al.* [1986], and *Stone et al.*, 1986])

$$j = 2.4 \times 10^6 (E/1.2)^{-1.12} \text{ cm}^{-2} \text{ s}^{-1} \text{ sr}^{-1} \text{ MeV}^{-1} \quad E \le 1.2$$

$$(4)$$

$$j = 2.4 \times 10^6 (E/1.2)^{-6.8} \text{ cm}^{-2} \text{ s}^{-1} \text{ sr}^{-1} \text{ MeV}^{-1} \quad E > 1.2$$

where E is in MeV. The thermal plasma density at this time was $n \approx 1$ cm^{-3} [*McNutt et al.*, 1987], so the minimum resonant energy, as estimated by the magnetic energy per particle, was $B^2/8\pi n \approx 0.12$ MeV. The stably trapped limit J^* should be compared to the equatorial omnidirectional integral flux J (>0.12 MeV), where we estimate

$$J(>0.12 \text{ MeV}) \approx 4\pi \int_{0.12}^{\infty} j \, dE = 1.0 \times 10^8 \text{ cm}^{-2} \text{ s}^{-1} \quad (5)$$

The factor 4π overestimates the integral over solid angle, but this error is compensated by the spacecraft location nearly 20° off the magnetic equator.

According to (3), the stably trapped limit at $L = 4.73$ is $J^* \approx 8.5 \times 10^6$ cm^{-2} s^{-1}, an order of magnitude less than J (>0.12 MeV). We conclude that the observed LECP electron fluxes near $L = 4.73$ are substantially in excess of the whistler mode stably trapped limit. Intense whistler waves should be excited by these energetic electrons and were in fact observed by the Voyager plasma wave experiment [Gurnett et al., 1986]. The whistler intensity at Uranus exceeded even that observed in the Io torus and was much greater than that observed at Saturn.

SPECTRAL PROPERTIES WITHIN THE CORE MAGNETOSPHERE

Figure 10 shows a number of different samples of the sector-averaged proton and electron spectra which occurred within the core magnetospheric regions. Proton spectra are shown along the top row, and the electron spectra sampled at the identical times are shown along the second row. The positions within the magnetosphere where the spectra were sampled are marked by the letters A–H above the proton and electron pressure profiles shown within the panel at the bottom of the figure.

The spectra shown in Figure 10 are quite complex. Characterizations of the spectral shapes within Jupiter's and Saturn's magnetospheres [Krimigis et al., 1981, 1983] have shown that the spectra can often be characterized with a so-called kappa distribution which has the characteristics of a power law at high energies ($j \propto E^{-\gamma}$) and those of a Maxwellian at lower energies ($j \propto E \exp(-E/kT)$). Alternatively, a single-sloped power law spectrum sometimes suffices, particularly with the electrons. With some notable exceptions, such characterizations are insufficient for the Uranian magnetosphere, and it is the higher-energy portions of the spectra that are often most peculiar. This point can be illustrated by considering an example. The proton spectrum at $\sim$1446 UT (spectrum D), for example, shows that as one moves to higher and higher energies the slope of the spectrum never settles to a single value but continues to become steeper and steeper. Such behavior is seen in a number of places in both the electrons and the ions. One might suspect that a single Maxwellian could fit the entire spectrum, but we show below that such is not the case. The proton spectrum at $\sim$1546 UT, in particular, shows an inflection at midenergies, suggesting the presence of two distinct non–power law spectral components. Among the proton spectra shown, the best exception to the rule is the spectrum sampled at $\sim$1749 UT (just outside the Miranda minimum L shell position) which appears to display a classical power law tail together with a Maxwellianlike rollover at lower energies. Within the electrons there are two spectra which approximate power law behaviors over the LECP energy range. They are the spectrum at $\sim$1838 UT sampled at the spacecraft minimum L shell position and inside Miranda (with a power law spectral index of $\gamma \sim 1.1$) and the spectrum at $\sim$2002 UT sampled outbound between Ariel and Miranda (with $\gamma \sim 1.8$). Additionally, the electron spectrum at $\sim$1749 UT (in the vicinity of the Miranda minimum L shell position on the inbound leg) appears to display Maxwellianlike behavior at the lower energies, contrary to the other spectra shown.

It is traditional in overview presentations, such as this paper, to display the spectral parameters as a function of time or position. Because the shapes of the spectra change both

quantitatively and qualitatively, we found it necessary to develop a new technique for the display of the spectral properties. If one takes the ratio of two adjacent energy channels (call them channels 1 and 2), one can obtain the spectral index γ or the temperature kT under the assumption that the spectral shape is power law $j \propto E^{-\gamma}$ or Maxwellian $j \propto E \exp(-E/kT)$, respectively. The energy bandwidths of the channels must be deconvoluted during the calculation. This procedure can be repeated with the next adjacent pair of energy channels (channels 2 and 3). If the true spectral shape is power law, the first determination of the spectral index γ_{12} will be approximately equal to the second γ_{23}, and the two temperature evaluations, kT_{12} and kT_{23}, will be inconsistent. This technique is illustrated by using actual low-energy electron results (<200 keV) shown in the bottom half of Figure 11. In this plot the circles correspond to the ratios of the two lowest-electron energy channels (22–35 keV and 35–61 keV) for deriving both a power law spectral index (the line of circles at the very bottom of the plot) and a Maxwellian temperature (the line of circles at the top of the lower panel of the figure). The solid lines correspond to similar calculations using the ratio of the next to the lowest pair of energy channels (35–61 keV and 61–112 keV). Similarly, the small pluses were generated with still higher energy channels.

From the clusterings of the lines on Figure 11 it is clear that prior to $\sim$1700 UT and after $\sim$1930 UT (i.e., $L \gtrsim 6$) the power law is a much more appropriate representation of the low-energy (<200 keV) electron spectral shapes than is the Maxwellian. Spectral indices range from about $\gamma = 3$ in the outer zones to about 1.5. The behavior in the vicinity of the minimum L shell positions of Miranda, however, is strikingly different. (The minimum L shell crossing times of all of the satellites are shown near the middle of the panel.) Just outside the Miranda location on the inbound leg, the lines corresponding to the power law representation flare dramatically apart, and the lines corresponding to the Maxwellian representation pinch together. A Maxwellian temperature of $kT \sim 30$ keV is indicated (also see electron spectrum F in Figure 10). At the outbound Miranda location the trend toward a Maxwellian is the same, but a full Maxwellian representation is not quite realized. Inside the location of Miranda the spectra are somewhat confused, showing neither pure power law nor pure Maxwellian behavior. Something very distinct must be happening in the vicinity of Miranda, causing the electron distributions to "thermalize." The whistler mode emissions reported by Gurnett et al. [1986] (particularly at 3.11-kHz frequencies) are substantially enhanced near and inside the orbit of Miranda, and future studies may reveal a connection between these, or other waves, and the thermalization events.

The top half of Figure 11 shows the spectral behavior of the more energetic electron channels (252–1200 keV) using the same format. Since a different physical detector is used for these channels than is used for the lower-energy channels, we chose not to mix the results from different detectors. We were therefore confined to three channels and only two ratios (and these are available only when the counts are well above background). Additionally, the effective geometric factor of the highest-energy channel is about a factor of 20 smaller than that of its adjacent channel (leading to a sensitivity to calibration inaccuracies). Hence in using these summary displays we are not quite as confident of our absolute characterizations of the spectral shapes for these channels (i.e., Maxwellian "here" and power law "there") as we are for the results discussed
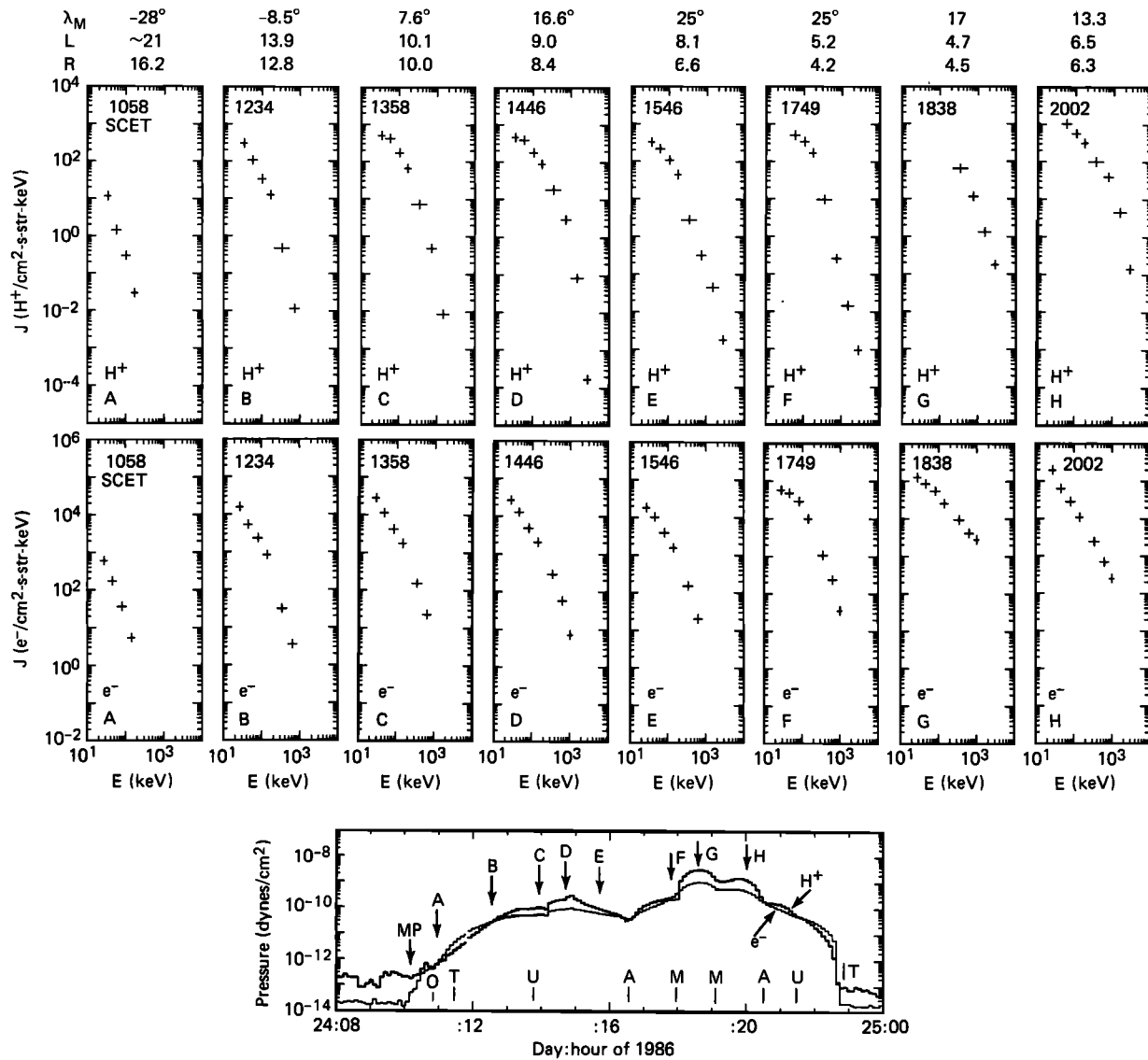
Fig. 10. Proton (top row) and electron (second row) differential intensity spectra (sector averaged) sampled at various positions within the "core" magnetosphere. Proton and electron spectra were sampled at identical times. The sampling times (A–H) are marked above the proton and electron pressure profiles shown in the panel at the bottom of the figure. That panel also shows the magnetopause position (MP) and the crossing times of the minimum L shell positions of the five major satellites (O, T, U, A, M). Radial position, L shell position (M. H. Acuña et al., submitted manuscript, 1987) and dipole magnetic latitude of the sampling times are shown above the spectra.

above and for the results to be discussed below concerning the ions. However, we are confident in the display's relative characterization of the variability of the spectral shapes. With these comments in mind, we can see from Figure 11 that there is considerable variability in the behavior of the energetic electron spectral shapes. Power law characterizations are often not appropriate, with notable exceptions being the regions inside the orbit of Miranda and the regions corresponding to the brief time near 2000 UT, between Miranda and Ariel on the outbound leg.

Figure 12 shows that the spectral behavior of the ions is far more complex than that found with the electrons. For the low-energy ions (<215 keV) a power law characterization is most appropriate prior to ~ 1300 UT and after ~ 2150 ($L \gtrsim 12$), with spectral indices ranging between 4 in the outer regions and 1.6–1.8 in the more planetward regions. Inside these positions the vertical lines mark the approximate transition times between different kinds of behavior. Maxwellian behav-

ior is favored (not precisely) between lines 1 and 2, lines 3 and 4, and lines 5 and 6, with other regions being either mixed or unspecified. Maxwellian temperatures between ~ 35 keV and ~ 50 keV are indicated where the Maxwellian characterization is appropriate.

At higher energies within the proton spectra ($E \sim 215$–3500 keV) there are several regions that are notably peculiar. In particular, a very high temperature Maxwellian spectral shape seems to best characterize the observed spectra in several regions. This behavior is most distinct on the outbound leg between 1930 and 2030 UT ($kT \sim 225$–250 keV), but it also occurred between 1400 and 1500 UT on the inbound leg ($kT \sim 125$ keV) and also for half an hour centered on ~ 2130 UT. In those regions where Maxwellian behavior is indicated at both low and high energies (e.g., 1400–1500 UT) the temperatures kT of the two components are quite different. We have no explanation for the Maxwellian behavior at very high energies (it could just represent transitions to power laws
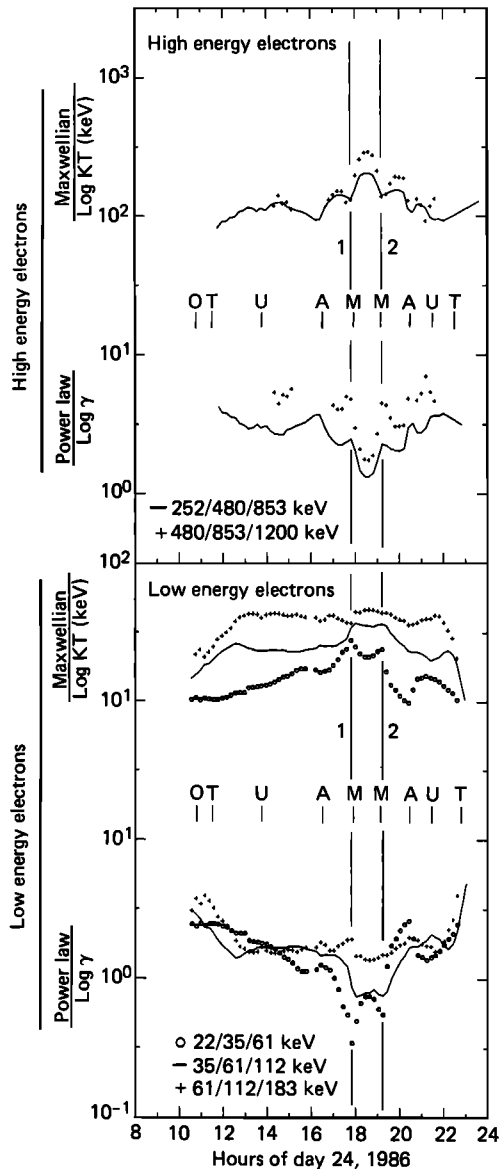
Fig. 11. Electron spectral properties. (Bottom) The four lowest LECP electron energy channels are used to derive three power law spectral slopes γ and three Maxwellian temperatures kT. One chooses the best representation of the spectral shape by noting which representation (power law or Maxwellian) causes the three lines to cluster closely together. Each line of symbols (circles, solid, pluses) is derived using the ratio of adjacent energy channel outputs. For instance, the circles are derived using the channels 22–35 keV and 35–61 keV (in the key these channels are shown with the format 22/35/61). (Top) An identical procedure was used for the high-energy portions of the electron spectra. See the text for further details. The crossing times of the minimum L shell positions of the five major satellites are shown in the middle of each panel.

and power law behavior at high energies) would suffice for the entire range of LECP proton energies. The clearest example of these regions lies between 1650 and ~ 1800 UT (between the Ariel and Miranda minimum L shell positions on the inbound leg); spectrum F of Figure 10, already noted for its kappalike behavior, is representative. We note that this region is also the region of "thermalization" of the electron spectra.

To a significant extent the behavior of the spectral characteristics of the low- and high-energy portions of the proton and electron spectra appears to be dictated by different mechanisms (i.e., the high- and low-energy components are decoupled). One reason may be the relative effects that satellite interactions have on the different components. As noted above, the flux minima at the satellite minimum L shells (see Figure 7) are more pronounced at high energies. Also, the

above our range of energies), and at this time we ascribe no particular physical significance to the Maxwellian behavior. In those regions of the high-energy proton spectra where power law shapes are indicated, the spectral indices range from 2.5 to 5. Note that there is one region, between 1530 and 1630 UT, which is most confused with respect to which spectral shape is most appropriate for this high-energy component. That region corresponds to the so-called "injection event" discussed earlier in reference to Figure 9.

There appear to be only a few regions in Figure 12 where a kappa distribution (with Maxwellian behavior at low energies
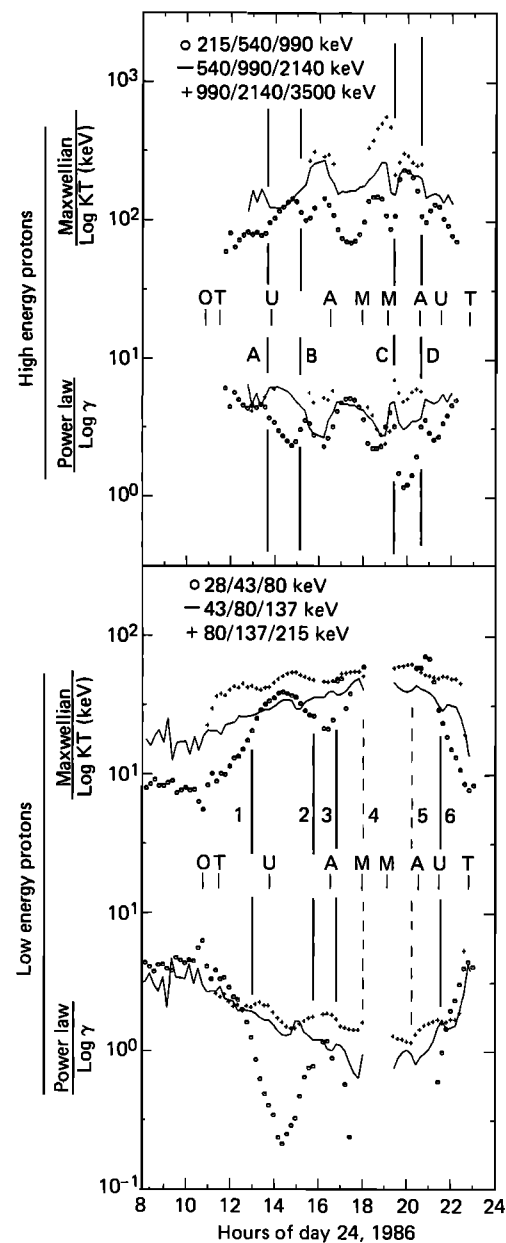

Fig. 12. Same as Figure 11, but for protons rather than electrons. The vertical lines are somewhat subjectively placed at some of the transition times between different kinds of spectral behaviors.
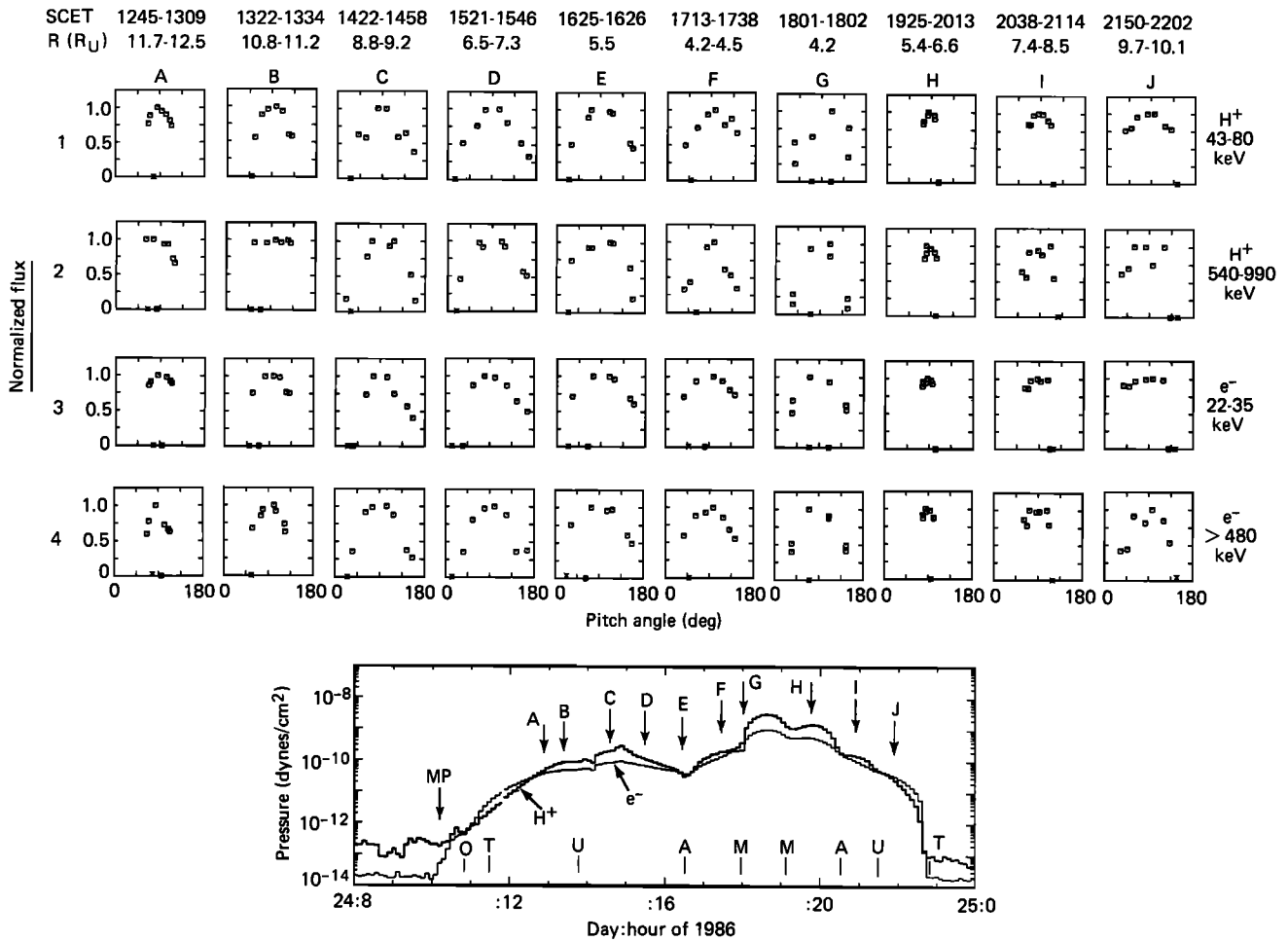
Fig. 13. Selected pitch angle distributions for low-energy protons (top row), high-energy protons (second row), low-energy electrons (third row), and high-energy electrons (fourth row). Within each column the distributions were not all sampled at identical times but were sampled within the range of times (and the range of radial positions) noted at the top of each column. The centers of the sampling times are marked above the proton and electron pressure profiles shown in the panel at the bottom of the figure. Also shown in the panel are the times of the magnetopause crossing (MP) and of the crossing of the minimum L shell positions of the five major satellites (O, T, U, A, M).

proton injection event shown in Figure 9 is likewise more pronounced at higher energies.

PITCH ANGLE DISTRIBUTIONS WITHIN THE CORE MAGNETOSPHERE

Figure 13 shows 48-s snapshots of the normalized pitch angle distributions sampled within the hard radiation regions of the Uranian magnetosphere. Within each panel, sector 8, the background sector, is marked with a star rather than with a square. The top two rows show low- and high-energy proton distributions, and the bottom two rows show low- and high-energy electron distributions. Along the vertical columns the distributions were not all sampled at identical times but were sampled at specific times within the range of times listed above each column. Because the spacecraft moved very rapidly in B-L space, even the relatively rapid 48-s pitch angle scans were not rapid enough to eliminate time variation disruptions of the pitch angle orderings (due to the spacecraft motion through spatial structures). Within the time spans listed above each column, the least disrupted distributions were selected, but some time variation perturbations remain within some of the distributions shown. Additionally, spatial gradients sensed by the finite Larmor radii of the ions have

also perturbed some of the pitch angle orderings within some of the proton pitch angle distributions. The centers of the times that correspond with the vertical columns are marked above the proton and electron pressure profile shown in the panel at the bottom of the figure.

Relatively well behaved and well developed trapped or "pancake" pitch angle distributions predominate within the Uranian magnetosphere at both low and high energies. Some such distributions are narrower, or more closely confined to 90°, than others, but before significance can be attributed to such features, Figure 2 should be consulted to determine the magnetic latitude (or the value of B/B_0) at which the particular measurement was made. For example, the relatively narrow distributions for some channels shown along column B in Figure 13 were sampled at just the magnetic equator, and so the narrowness there may well be a significant feature. In particular, we noted in an earlier section that our conclusions concerning the value of the plasma β parameter in the vicinity of the magnetopause might be sensitive to the fact that the spacecraft encountered the magnetopause at very high magnetic latitudes. The pitch angle distributions shown along column B support that assertion. If the populations at the magnetic equator in the vicinity of the magnetopause were as
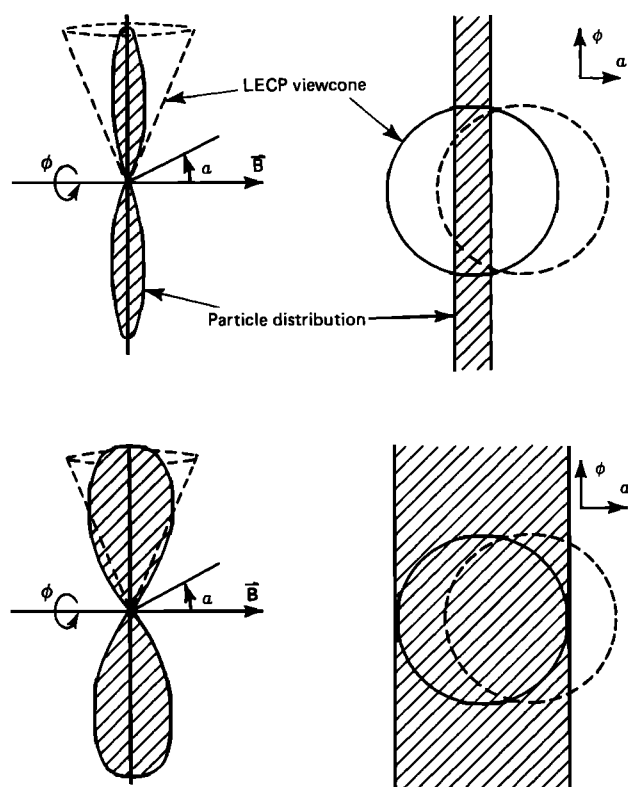
Fig. 14. Illustration of the response of the relatively broad view cone of the LECP detector to a comparably broad (bottom row) or very narrow (top row) trapped or pancake particle pitch angle distribution. The left column shows a side view of the relative breadths, and the right column shows a "down the detector throat" visualization of the convolution between the particle distributions and the detector response. The parameters α and ϕ are angles.

narrow as some of those shown along column B, then Figure 2 (top) shows that none of those populations would be visible to the spacecraft at its entrance position. Future encounters may well find the low magnetic latitude Uranian magnetopause to be a high-β structure.

One additional important issue that we will address with Figure 13 is the dramatic inbound/outbound flux asymmetry noted in the discussion of Figure 7 (occurring most prominently near $L \sim 6.5$ within the 540- to 990-keV proton channel). It was hypothesized during that discussion that the asymmetry was due to the fact that the spacecraft was closer to the magnetic equator during the outbound path and that the dramatically enhanced fluxes observed during the outbound pass were confined particularly close to the magnetic equator. A rough calculation showed that the pitch angle distribution of the enhanced outbound fluxes must be confined exclusively to within 45° of the 90° position (i.e., between $\alpha = 45°$ and 135°).

The relevant pitch angle distribution in Figure 13 is the one designated H in the second row. One notes immediately that at that location there is only a very poor sampling of the entire range of pitch angles (77°–103°). However, one sees also that even within that very narrow range of pitch angles the distribution appears to fall rapidly as a function of pitch angle away from the 90° position. There does appear to be some variability, but an examination of adjacent measurements in both time and energy channels show that the distribution selected is representative of this location.

Crucial to interpreting this pitch angle distribution is the

realization that the view cone of the LECP detectors is relatively broad ($\pm 22°$ with a ramped falloff in the effective area beyond $\sim \pm 19°$). Thus it is somewhat surprising that within $\pm 13°$ in pitch angle the fluxes could, under any circumstances, vary as much as they do. However, unlike the case when one is trying to resolve a narrow loss cone, we are trying here to resolve the width of a "slab" in angle space rather than a "point" or a "circle." This point is illustrated in Figure 14. The illustrations on the left side show two hypothesized particle pitch angle distributions (shaded) as they would be compared to the LECP view cone. The particle distributions are assumed to be symmetric about **B**. The illustrations on the right side show views looking "down the throat" of the LECP view cones, and from this perspective the particle distributions look like slabs. One can visualize that the response of the LECP detector corresponds to a convolution between the solid angle of the distribution and the solid angle of the view cone. If one moves the LECP view cone, say from the solid circles to the dashed circles on the right-hand panels, then the LECP response does change even if the movement is substantially less than the size of the view cone. Both of the situations shown, with the particle distribution much narrower than the view cone and a distribution of comparable width to the width of the view cone, will give rise to a $\sim 20\%$ variation in the LECP response (as is observed) for a $\pm 13°$ motion of the position of the view cone. The distribution, however, can be no broader than the size of the view cone.

If the shape of the distribution is a step function (i.e., $f(\alpha) = 1$ for $90° - \varepsilon < \alpha < 90° + \varepsilon$, and $f(\alpha) = 0$ elsewhere), a deconvolution procedure shows that the response shown in Figure 13 (row 2, column II) constrains the particle distribution to being no wider in pitch angle than about 20° from the 90° positions. If we now assume that the distribution has a $\sin^n (\alpha)$ shape and that $\sin^n (90° - 20°) = 0.5$, we obtain $n \simeq 11.2$. Then it is easy to show that the flux to be measured at $\alpha \sim 45°$ will be 2 orders of magnitude below the flux at $\alpha \sim 90°$. As these particles drift around to the frontside along constant L shells, this 45° flux at the outbound location will end up at $\alpha = 90°$ at the inbound location of the spacecraft observation point. Hence the inbound fluxes will appear to be low by 2 orders of magnitude. If we assume that $\sin^n (90° - 20°) = 0.25$, we obtain $n \simeq 22.2$ and a flux contrast between the inbound and outbound positions at well over 3 orders of magnitude.

The observations and rough calculations given above are highly suggestive that the populations observed outbound near $L \simeq 6.5$ (between the minimum L shell positions of Miranda and Ariel) were highly confined to the equatorial regions. This confinement could explain the apparent dramatic inbound/outbound asymmetry as an artifact of how the magnetosphere was sampled. The evidence is certainly not conclusive that a factor of > 1000 in asymmetry can be explained, since "shoulders" could exist within the unsampled regions of the pitch angle distribution. However, the detector response shown in Figure 13 can only occur if those particles that are observed are part of a population that is substantially constrained near the 90° pitch angle region. Also, despite indications discussed earlier that injection phenomena are occurring, it is easier to accept a rather peculiar pitch angle distribution than it is to accept the kinds of dramatic magnetospheric dynamics that would have been required if the asymmetry had turned out not to be an artifact.

The energetic electron pitch angle distribution sampled at the same time (row 4, column H on Figure 13) suggests that

these energetic electrons are also confined fairly closely to the magnetic equator, although perhaps to a lesser degree than are the protons. The electrons also displayed a substantial inbound/outbound asymmetry, although Figure 8 shows that asymmetry to be 1 order of magnitude rather than the >3-orders-of-magnitude asymmetry found with the protons. (In Figure 8, compare the energetic channel fluxes at 1720 and 1945 UT.) A lesser inbound/outbound asymmetry is certainly consistent with a lesser equatorial confinement; however, the very limited pitch angle coverage available at the outbound position allows us little room for making quantitative distinctions between asymmetries of 1 and 3 orders of magnitude.

THE URANIAN MAGNETOTAIL

Figure 15 shows some details of the LECP data taken within the Uranian magnetotail and within the dawnside magnetosheath. The second panel shows the count rate response of the lowest-energy proton and electron channels. The third panel shows the total integrated proton and electron pressures. The fourth panel shows the power law spectral index of the energy spectra derived using the lowest two proton energy channels. The coverage in this bottom panel is sporadic because it was required that the fluxes in both channels be a factor of 2 above their respective backgrounds (the backgrounds were subtracted). The top panel shows, in the form of "whisker" vectors, the directions ϕ_1 and magnitudes a_1 of the first-order angular anisotropies within the lowest-energy proton channel (recall that the normalized scan plane rates are fit to the form $a_1 \cos (\phi - \phi_1)$). The approximate directions of the Sun and of Uranus are shown to the left of the top panel. Those whiskers that are shown with a dashed line correspond to scans where the highest count rate observed in any sector was below 2 c/s. (Background rates, which have been subtracted for the purposes of the angular fittings, were typically of the order of $\sim$0.6 c/s). The second panel of Figure 3 shows how the solar ecliptic sky was being sampled by the scanning LECP detectors prior to $\sim$1230 UT on day 25. The third panel of Figure 3 shows how the "sky" was sampled after 1230.

Within the second and third panels of Figure 15 are shown the time positions where the Voyager magnetometer detected neutral sheet crossings [Ness et al., 1986] (labeled N1–N4). Also shown is the magnetopause crossing location reported by the plasma team [Bridge et al., 1986] (labeled MP). Proton activity is clearly present in the intervals around all of these marked features, but it is significant that the proton enhancements are not necessarily symmetric with respect to the neutral sheet crossings. Also, there are particle enhancements that are separated significantly in time from the neutral sheet crossings. Note in Figure 1, for example, that while the first neutral sheet crossing occurred at a low dipole magnetic latitude of $\lambda \sim 8°$, the first significant impulsive proton event shown in Figure 15 (at $\sim$0300 UT on day 25) occurred at a dipole magnetic latitude of $\sim$43° (see Figure 2), spatially very removed from the point of observation of the neutral sheet. This particular high-latitude ion event also occurred fairly close to the planet, at a radial distance comparable to the frontside magnetopause standoff distance. In some regions the detached proton enhancements, and even the flux values within the attached enhancements, appear to be sporadically repetitious with a characteristic time scale of the order of 1 hour. It is significant that the most intensive proton enhancement occurred in association with the very last neutral sheet crossing (N4, $\sim$0000 UT on day 26), a crossing that is de-

scribed by the magnetometer team as being a "partial" crossing.

The electron fluxes obviously behaved very differently. The intensity of the electron enhancements is a very strong function of the distance down the tail; indeed, only the first two neutral sheet crossings show clear electron enhancements. There is the hint of an enhancement during the last neutral sheet crossing.

In reference to the pressure profiles in the third panel, a comparison with Figure 1 of Ness et al. [1986] shows that these particle pressures were generally insignificant for pressure balance considerations (see Behannon et al., [this issue] for a full discussion of the pressure balance considerations within the magnetotail, including the LECP contributions). For the first three neutral sheet crossings the local β parameters and the ratios of the neutral sheet particle pressures to the lobe magnetic field pressures (call those ratios β'), were of the order of 0.1 and 0.01, respectively. For the last neutral sheet crossing the local β was >1; however, the parameter relevant to the pressure balance considerations, β', was still only $\sim$0.14. Of course, extrapolations of the LECP energy spectrum to lower energies could alter the situation with regard to this last crossing.

The whiskers illustrating the first-order proton anisotropy (top of Figure 15) obviously show a tremendous amount of variation. Pursuant to our earlier discussions, one might expect both particle streaming and spatial pressure gradients to contribute to these variations. Indeed cases of both strong gradient anisotropies and strong particle streaming anisotropies are found. The reader should note that if the magnetotail of Uranus consists of a time-stationary, spatially planar neutral sheet oriented as discussed in reference to Figure 1, and if that neutral sheet is populated with a similarly time-stationary (nonstreaming), spatially planar plasma sheet population, the anisotropy vectors would all point approximately perpendicular to the vector pointing toward Uranus, and they would all point in one direction (either left or right) throughout each neutral sheet crossing. (Note that both the directions of the spatial gradients and the directions of B change as the spacecraft crosses the neutral sheet, leading to whiskers that point in the same direction before and after the crossing.) Given the polarity of the magnetic lobes and the orientation of the spacecraft [see Ness et al., 1986, Figures 2 and 5], one would expect the whiskers in the vicinity of the N1 and N3 neutral sheet crossings to point rightward (toward the $\sim$1:30 position on a 12-hour clock dial), and in the vicinity of N2 the whiskers should point leftward (toward the $\sim$7:30 position on a clock dial). There are whiskers in the vicinity of the N2 and N3 crossings emulating this expected time-stationary, planar behavior, but it is clear that there are many whiskers throughout that do not emulate that behavior. In many cases these "anomalous" whiskers correspond to ion streaming events, as is demonstrated for a few examples in Figure 16.

Figure 16 shows pie plots and some pitch angle distributions for seven different locations within the magnetotail (the approximate locations are marked in Figure 15 above the whisker panel). The left column of Figure 16 presents pitch angle distributions for the low-energy, 28- to 43-keV, proton channel (the stars correspond to the uncorrected background sector 8). The central column presents pie plots for the same low-energy proton channel, and the right-hand column presents pie plots for the next to lowest proton energy channel, 43 to 80 keV. The directions of the local field lines projected onto
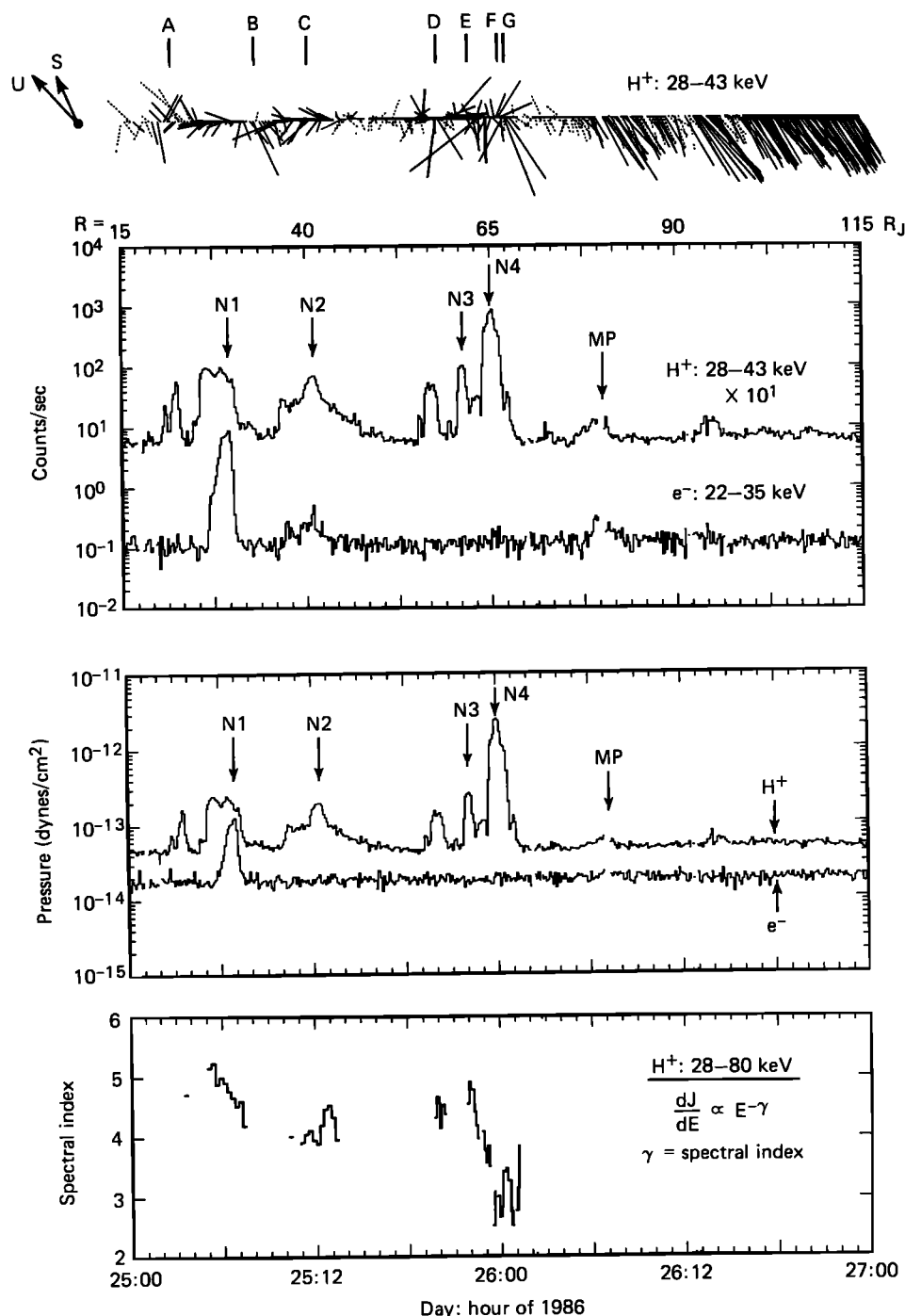
Fig. 15. The fourth or bottom panel shows the spectral index (defined in the figure) of the 28- to 80-keV protons within the Uranian magnetotail. A criterion of flux >2 times background was enforced for both channels used. The background was subtracted. The third panel shows the total integrated electron and ion pressures sampled within the Uranian magnetotail and within a portion of the downstream magnetosheath regions. The second panel shows the count rates from our lowest-energy proton and electron channels for the same time period. The top panel shows the first-order angular anisotropies within our lowest-energy proton channel. The "whisker" vectors shown have lengths proportional to the anisotropy amplitudes a_1, and they point in the direction ϕ_1 of the anisotropy (scan plane rates are fit to the functional form $a_1 \cos (\phi - \phi_1)$). The directions to Uranus and to the Sun are shown to the left of the whisker panel. Within the middle two panels are shown the times of the magnetic field neutral sheet crossings (N1–N4) [Ness et al., 1986] and the time of the magnetopause crossing (MP) [Bridge et al., 1986]. The seven labeled tick marks above the whisker panel show the approximate sample times used for Figure 16.

the LECP scan plane are shown on the middle panel pie plots. Also, the directions toward Uranus and toward the Sun are shown at the lower left of the figure.

The top row in Figure 16 (row A) shows, for the lowest-energy channel, a clear example of ions streaming toward Uranus and along the local field line. The principal evidence that favors a "streaming" interpretation over a "gradient" interpretation is the pitch angle distribution, which shows that the peak sector looks directly along the field line, with the largest flux occurring for particles moving parallel to B and
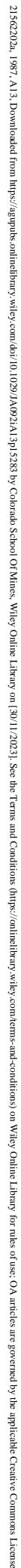
Fig. 16. Angular anisotropy "pie plots" (right two columns) and sector pitch angle plots for the seven time periods (rows A–F) marked above the "whisker" plot in Figure 15. On the pie plots the radial extents of the pie sections correspond to the normalized intensities of the fluxes within our eight angular sectors. The middle column corresponds to our lowest-energy proton channel (28–43 keV), and the right column corresponds to our next lowest energy proton channel (43–80 keV). The pitch angle plots in the left column are for the lowest-energy proton channel. The directions toward the Sun and toward Uranus are shown at the lower left. The projections of the magnetic field directions onto the LECP scan plane are shown along the middle column. On the pie plots, sector 8, the sector looking straight up, has been filled in with a biharmonic fit to the other seven sectors. On the pitch angle plots, sector 8 (not filled in but as it actually reads) is shown with a star rather than a square.

the smallest flux for particles moving antiparallel. The higher-energy channel shows a bidirectional anisotropy, but this type of inconsistent behavior between adjacent energy channels is quite common for energetic proton streaming events within the Earth's magnetotail [*Williams*, 1981; *Mitchell*, 1987]. The higher-energy channel may be viewing a streaming component plus a component being reflected back from a magnetic mirror located close to the planet. Velocity filtering effects play a crucial role in determining what energies will be seen. This streaming event occurred at the leading edge of the large impulsive event in Figure 15 that peaks at about 0340 on day 25. A close examination of the whisker vectors (Figure 15) that occur right at the peak of this event shows that the planetward streaming disappeared, only to reappear at the trailing edge of the event (however, the scan occurred after the counts became quite low, and so the anisotropy vector is shown with a dashed line).

The second row in Figure 16 shows a case of even more dramatic streaming, but this time the streaming is in the tailward direction. Again the pitch angle distribution provides the crucial evidence for a streaming interpretation. The pie plot for the more energetic protons shows very different behavior, perhaps due to gradient effects, but the peak count rate is very close to this channel's background rate (0.6 c/s—this background has been subtracted). This anisotropy event was observed (Figure 15) in a region of persistent tailward flow imbedded within the relatively low flux regions between the first two neutral sheet crossings. Figure 1 shows that between those two crossings the spacecraft never moved very far away from the neutral sheet position.

The third row in Figure 16 (row C) shows an example of the gradient anisotropies expected for a time-stationary/spatially planar plasma sheet structure. The fluxes peak near 90° pitch angle, and the higher-energy channel shows a somewhat more substantial anisotropy. This event was sampled in the vicinity of the second neutral sheet crossing (N2; Figure 15).

Rows D, E, and G of Figure 16 show further examples of dramatic tailward, field-aligned streaming sampled, respectively, (1) at the trailing edge of the detached proton enhancement event centered near 2000 UT, (2) at the trailing edge of the enhancement associated with the third neutral sheet crossing, and (3) at the trailing edge (associated with the trailing enhancement) of the very dramatic proton enhancement associated with the fourth neutral sheet crossing.

Finally, row F of Figure 16 shows a clear example of a spatial gradient anisotropy sampled during the ion enhancement associated with the fourth neutral sheet crossing. This anisotropy persists for a number of angular scans (6.4 min/scan at this time). Given the direction of $\hat{b}$ shown in Figure 16, the gradient direction inferred from the anisotropy suggests that the bulk of the hot plasma lies toward the ecliptic south from the spacecraft position. And indeed one expects that at this observation time the plasma sheet population should be just south of the spacecraft's position, having just passed from a northward to a southward position at the time of the N3 neutral sheet crossing (see, for example, Figure 5 of *Bridge et al.* [1986] or our Figure 17, discussed in the next section). Our observations are consistent with the plasma sheet/neutral sheet structure having warped up to (or having thickened to encompass) the spacecraft position. Note, however, that the flux values are an order of magnitude higher than the values observed within the neutral sheet regions (at N3) just 2 hours before.

By generalizing the information extracted from Figure 16 to

other anisotropy vectors shown at the top of Figure 15 it is clear that field-aligned proton streaming is an extremely common feature of the Uranian magnetotail, just as it is with the Earth's magnetotail (see Figure 17, which summarizes our observations). Also, the anisotropy vectors in Figure 15 give the distinct impression that the field-aligned streaming is most prominent at the edges of the proton enhancements rather than at the centers of the proton enhancements. Planetward streaming is observed at the edges of the detached enhancement near 0340 UT on day 25, and also at the leading edge of the enhancement associated with the N1 neutral sheet crossing. Tailward streaming is observed between the N1 and N2 associated enhancements, and planetward streaming appears to return at the trailing edge of the N2 enhancement. In association with the more distant neutral sheet crossings, tailward streaming predominates at the edges of the enhancements, with the exception of the leading edge of the detached enhancement centered near 2000 UT on day 25, where planetward streaming occurred. Gradient anisotropies, or anisotropies that are small and confused, appear to predominate in the regions closest to the actual magnetic neutral sheet crossings. In the vicinity of the N1 crossing (unlike the other crossings) the gradient anisotropies appear to have pointed in the wrong direction, given our simple, time-stationary, planar model of the neutral sheet. However, as the second panel of Figure 3 shows, the LECP scan plane did not lie parallel to the ecliptic plane at this time, and a warping of the neutral sheet plane could reverse the direction of the gradient anisotropy whiskers. Alternatively, the reversed gradient anisotropies could have resulted from a cross-neutral-sheet temperature variation that gives rise to an outward (away from the neutral sheet) pressure gradient, despite the presence of an inward density gradient. Such reversed pressure gradients have been observed within the Earth's magnetotail in the regions closest to the Earth (D. G Mitchell, private communication, 1986).

The energetic ion streaming behavior occurring predominantly near the boundaries of the Uranian magnetotail plasma sheet enhancements is highly reminiscent of the occurrence of ion streaming at the boundaries of the Earth's plasma sheet population, forming the so-called plasma sheet boundary layer [e.g., *Eastman et al.*, 1984; *Williams*, 1981]. The variability in streaming direction observed at Uranus is quite common within the Earth's magnetotail. Velocity filtering effects, magnetic mirroring of planetward streaming ions, and (according to some authors) variability as to the location of acceleration regions with respect to the spacecraft position are all thought to play roles in generating such variability. It is argued by *Eastman et al.* [1984] that the Earth's plasma sheet boundary layer is the dominant site in terms of the transport of energy and mass within the magnetotail. The clear analogies in terms of observational phenomenology that exist between the Uranian and terrestrial plasma sheet boundary layers suggest similarities in the energization and transport mechanisms.

Given the sporadically impulsive nature of the proton enhancements within the magnetotail and given the temporal distortions in the plasma sheet geometry associated with those enhancements (note in Figure 17 the very substantial spatial separations between the "average" plasma sheet/neutral sheet structure and the sporadic LECP ion enhancements; see also *Behannon et al.*, [this issue]), it is quite clear that the magnetotail of Uranus is a temporally dynamic environment. Coupling that characteristic together with the similarities between the Uranian and terrestrial magnetospheres in terms of the
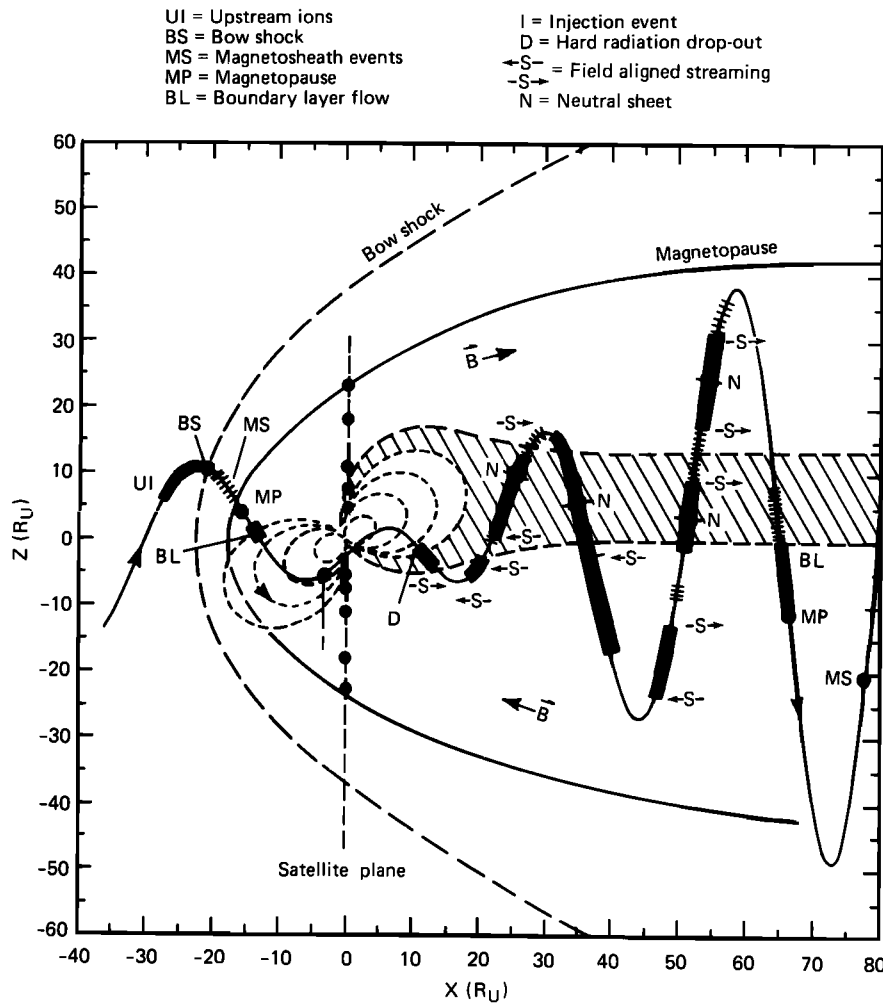
Fig. 17. Summary of selected LECP observations and the Voyager 2 trajectory at Uranus displayed in a rotating, solar magnetospheric coordinate system. The X axis is parallel to the Sun-Uranus line, and the X-Z plane is coplanar to the planetary magnetic dipole moment vector $\mathbf{M}$. Dipole magnetic field line shapes are shown for dipole L shell values of 5, 10, 15, and 20 R_U. The bow shock and magnetopause positions and shapes were borrowed from the conical sections given by *Bridge et al.* [1986], where cylindrical symmetry is assumed. The boundaries shown should be considered as only approximately positioned. The circles positioned on the "satellite plane" mark the radial extents of the five major Uranian satellites and are not intended to denote the instantaneous positions of the satellites. Tailward of ~20 R_U on the outbound portion of the trajectory, the width and position of the shaded region corresponds to the average plasma sheet structure determined by *Bridge et al.* [1986] for the <6-keV plasmas. The positioning of the plasma sheet "horns" was guided by LECP observations of the energetic plasma sheet components at high latitudes. Various LECP observations are indicated with labeled thickenings, shadings, or circles on the spacecraft trajectory. The labelings can be decoded using the key above the figure. Those thickenings and shadings within the magnetotail which are not explicitly labeled correspond to observations of the high-energy component of the plasma sheet population. With respect to the plasma sheet observations, the solid thickenings correspond to the very intense fluxes, and the clustered tick marks correspond to less intense fluxes.

plasma sheet boundary layer streaming characteristics, it is extremely tempting to suggest that substormlike processes are occurring within the magnetotail of Uranus. However, plasma sheet boundary layer particle streaming at Earth occurs even in the absence of substorm activity [*Williams*, 1981; *Eastman et al.*, 1984], and the temporal dynamics might conceivably be attributed to other processes, such as the occurrence of large-scale "flapping" of the neutral sheet plane associated with macroscopic boundary wave activity.

The characteristics of the proton fluxes observed during the very last (N4) neutral sheet crossing, however, strongly favor a substorm interpretation. The fluxes associated with that crossing were an order of magnitude greater than the fluxes observed in the vicinity of the neutral sheet just 2 hours before (at ~2200 UT). Even more significant is the behavior of the spectral index shown in the bottom panel of Figure 15. Throughout all of the ion activity observed in Figure 15 prior

to the N4 encounter, the spectral index remained consistently between 4 and $\gtrsim 5$. Just in association with the N4 crossing the spectral index dramatically hardened to $\gamma \sim 3$, indicating that the population is not only more intense but more energetic (per particle) as well. The point is that this last encounter with the plasma sheet population was not just a reencounter with the previously encountered plasma sheet population. The N4 population was distinct and was new. As Figure 17 shows, this distinct population was observed well away from the nominal plasma sheet position. However, the ion event observed at ~2000 UT in Figure 15 was observed just as far away from that nominal position as was the N4 event, and yet the 2000 UT event looked just like a simple reencounter with the "nominal" plasma sheet populations. Given the many similarities between the Uranian and terrestrial magnetospheres in terms of observational phenomenology and given the special properties of the N4 ion populations, we

attribute the N4 ion activity as having been generated by substormlike processes.

There are several other features of note in Figure 15 that should be addressed. The ion enhancement in the vicinity of the magnetopause shows first-order anisotropies just inside the magnetopause that parallel the clear magnetosheath flow anisotropies. As with the near inbound magnetopause observations, a boundary layer flow region is present in these outbound regions. It is of interest that the electrons show a feature within the same region. Such a "layer" of electrons in the vicinity of the magnetopause is commonly observed at Earth and forms a population distinct from the plasma sheet [Meng and Anderson, 1970; Meng et al., 1979].

The feature that occurs at ~1400 UT on day 26 is also of interest in that the anisotropy vectors grow in length and tilt slightly, as if these protons were coming from the magnetopause surface. The relative absence of electrons suggests that this enhancement is not just a reencounter with the magnetopause regions. These protons may have been plasma sheet particles escaping into the magnetosheath.

SUMMARY AND DISCUSSION

We have discussed a very broad range of magnetospheric phenomena in this paper, in order to present a relatively detailed overview of Voyager LECP observations in the Uranian magnetosphere. Figure 17 summarizes a number of the LECP findings and is useful for placing them within the context of the entire magnetospheric encounter. The coordinate system is a rotating, solar magnetospheric system with the X axis parallel to the Sun-Uranus line and with the X-Z plane containing the magnetic dipole moment vector. Further details are given in the caption for Figure 17.

Upstream Enhancements

Upstream of the inbound bow shock crossing, very intense upstream ions were observed that streamed rapidly in a direction tangential to the magnetospheric surfaces. Given the location of the spacecraft, the source of the ions was likely the nose regions of the magnetosphere. We have hypothesized that these ions could have represented the leftover remains of magnetosheath populations after the bow shock had moved planetward. The energy density of the (>28 keV) ions was, at times, large in comparison to the magnetic energy density but small in comparison to the thermal energy density of the solar wind (extrapolations to energies less than 28 keV could alter this latter comparison). Observations of upstream and downstream ions at more distant positions are discussed by S. M. Krimigis et al. (submitted manuscript, 1987), who present evidence that the source of the ions is leakage out of the magnetosphere. Relevant to this conclusion, we have noted on the outbound trajectory a proton enhancement that has characteristics suggestive of leakage of the magnetotail plasma sheet populations.

Magnetopause

In the vicinity of the inbound magnetopause the expected pressure gradient anisotropies were observed at times, but in general the first-order anisotropies were quite variable. Further analysis will probably reveal either that the surface of the magnetopause was extremely variable or that the magnetopause is an active site for energization and transport. Inside the magnetopause a convectively flowing (>200 km/s) boundary layer was observed. A convective boundary layer

was also observed just inside the outbound magnetopause location.

Satellite and Other Inner Region Signatures

Within the core, or hard radiation regions, the higher-energy electron and proton fluxes display distinct minima near some of the satellite minimum L shells. It was shown that for the energetic electron features the latest multipole expansion magnetic field model of M. H. Acuña et al. (submitted manuscript, 1987) and Connerney et al. [this issue] substantially improves the orderings with respect to the minimum L shell positions of the satellites over the orderings obtained using the original offset tilted dipole model of Ness et al. [1986]. The new orderings are not exact, but it remains to be determined whether the explanation lies with inaccuracies in the field model or with temporal variations in the trapped populations. The features within the energetic ions are not nearly as well ordered as are the energetic electron features. The lack of ordering with respect to the minimum L shell positions may be due in part to sensitivity to the "real-time" locations of the satellites (relative to the spacecraft location). However, some energetic ion features appear to have required temporally dynamic (e.g., substorm injection) effects. These topics are addressed further below and by Cheng et al. [this issue]. The low-energy ions and electrons appear to be far less influenced by the satellites, and relatively rapid radial transport is presumably smearing out the features that should otherwise form.

Particle Moments, Stably Trapped Limit, and Shielding of Convection

The energy density of the LECP ions and electrons within the core magnetosphere is far below the magnetic energy density (the maximum $\beta \sim 0.13$), so that this magnetosphere can probably be considered a "vacuum" magnetosphere for the purposes of understanding the global magnetospheric configuration. One caveat to that conclusion is the finding of well-developed pancake-type pitch angle distributions near the magnetic equator on the inbound pass, suggesting that important populations may not have been observable just inside the magnetopause because of the spacecraft's high magnetic latitude. We cannot exclude the possibility that the low-latitude, dayside magnetopause region is a high-β region.

Despite the appearance of "emptiness" on the basis of particle pressures, in other senses this magnetosphere is not empty at all. In particular, the electron fluxes exceed the whistler mode stably trapped flux limit by ~1 order of magnitude in the inner regions, despite the presence of very substantial whistler mode wave activity. A strong source of energetic electrons is evidently required. Electron injection into the inner magnetosphere is also indicated by the phase space density profiles [Cheng et al., this issue].

In order to understand shielding of plasma convection within the Uranian magnetosphere it is important to establish which populations dominate in terms of overall energy density, i.e., the LECP measured populations at $E \gtrsim 28$ keV or the populations observed at much lower energies, $\lesssim 6$ keV. Preliminary estimates indicate that within the middle and inner magnetosphere ($L \lesssim 18$ R_U) the LECP energy densities are greater than the energy densities observed at lower energies at all radial distances near the magnetic equator. This fact will have to be incorporated into any models of shielded convective transport. This issue is discussed further below.

Energy Spectra

The spectral properties of ions and electrons within the core magnetosphere are extremely complex. The low-energy portions ($E \lesssim 200$ keV) appear to behave differently from the high-energy portions. At low energies the electrons generally exhibit power law behavior with the notable exception of a dramatic "thermalization" in the vicinity of the minimum L shell position of Miranda. An association with enhanced plasma wave activity near and inside Miranda is suggested. The low-energy ions show both power law behavior in the outer regions ($\gamma \sim 1.5$–4) and Maxwellian and mixed behaviors in the inner regions ($kT \sim 35$–50 keV). The high-energy ions (~ 200–3500 keV) are at times best characterized with a Maxwellian shape, with a temperature parameter kT ranging between 125 and 250 keV. The temperatures of the high-energy component are always distinct from the temperatures of the low-energy component. The high-energy proton components at other times are best characterized with power laws, with spectral (γ) parameters ranging between 2.5 and 5. Only in a few regions can the entire energy range of the LECP spectra be satisfactorily represented with the so-called kappa distribution for protons or with a one-slope power law distribution for electrons.

Pitch Angle Distributions

The pitch angle distributions within the core magnetosphere generally show well-developed trapped or pancake distributions for both low- and high-energy ions and electrons. Between the outbound minimum L shell positions of Miranda and Ariel the pitch angle distributions show that a substantial population is confined particularly close to the magnetic equator, with the pitch angle distribution being generally confined between $\alpha = 70°$ and $110°$. If that confinement is particularly extreme (i.e., with fluxes in the vicinity of $\alpha = 45°$ being 3 orders of magnitude lower than the fluxes at $\alpha = 90°$), then a dramatic inbound/outbound flux asymmetry between the Miranda and Ariel portions of the magnetosphere can be explained as an artifact of the sampling of these magnetospheric regions. In general, despite the evidence for injection phenomena elsewhere, it is more palatable to accept the presence of a peculiar pitch angle distribution than it is to accept the kind of extreme dynamics that would be implied by the flux asymmetry.

Magnetotail

The magnetotail of Uranus is an extremely active place. Proton and electron enhancements are observed in the periodically encountered neutral sheet crossings, but additionally, impulsive and sporadic proton enhancements are observed well detached in time and position from the identified neutral sheet crossings. A sporadic repetition characteristic time scale for these impulsive enhancements is of the order of 1 hour. The angular anisotropies reveal dramatic and highly variable field-aligned proton streaming predominantly on the boundaries of the proton enhancements. These streaming characteristics are reminiscent of the streaming observed within the plasma sheet boundary layer of the Earth's magnetotail. Both planetward and tailward streaming is observed. At Earth the plasma sheet boundary layer is a predominant site for the transport of mass and energy [*Eastman et al.*, 1984]. Thus the energization and transport processes occurring within the Uranian magnetotail would appear to be similar to those occurring within the Earth's magnetotail. The angular anisotropies also revealed, by sensing pressure gradients, that in several places the geometry of the plasma sheet structure became highly distorted or warped.

The clear analogies between the Uranian and the terrestrial magnetotails in terms of observational phenomenology, and the special properties of one particular "plasma sheet" encounter (day 26, 0000 UT), strongly suggest that substormlike processes are occurring within the Uranian magnetotail. With this conclusion it is them even more likely that processes similar to substorm injection also create some of the disorder that exists within the energetic ion populations of the quasi-dipolar regions. Special note is made of the peculiar energetic ion "injection" feature centered near 1545 UT in Figure 9 (with no corresponding feature occurring in the electrons in Figure 8). The position of this injection is shown in Figure 17. Further discussions can be found in the work by *Cheng et al.* [this issue]. In particular, the phase space densities derived by *Cheng et al.* [this issue] show a minimum in the regions adjacent to the injection feature, which can be generated if the dynamical processes introduce very substantial, time dependent azimuthal asymmetries. Substorm injections at Earth certainly generate such asymmetries.

Before leaving the discussion of the magnetotail regions, there is one feature that deserves further comment. It was noted in the discussion of Plate 1 that a plasma sheet–like population was observed immediately following the sharp dropout in the hard radiation population near 2240 UT on day 24. In Figure 17 that population corresponds to the thickened portion of the spacecraft trajectory just following the location marked "D." From the positioning in Figure 17 this population appears to correspond to the so-called "horns" of the plasma sheet populations, indicated with the shading on the figure. This population is similar to the other plasma sheet encounters in having field-aligned streaming associated with it. The anisotropy whisker vector that occurs near 2325 UT in Figure 5 corresponds to a tailward, field-aligned streaming condition.

Particle Transport

A key question that arises when dealing with any magnetosphere is how particles are transported from one region to another. With regard to the more energetic particles, this question is often posed within the framework of particle diffusion theory. To the extent that diffusion theory is valid, one may be able to draw analogies between the Uranian magnetosphere and the magnetospheres of Earth, Jupiter, and Saturn, despite the unique characteristics of the Uranian system. Questions of the more energetic particle transport are addressed for Uranus by *Cheng et al.* [this issue], who use the particle phase space densities to study sources, sinks, and transport processes.

Unlike the cases of the magnetospheres of Jupiter and Saturn, a number of investigators have been very quick to draw analogies between the Uranian and the terrestrial magnetospheres with regard to the transport of the lower-energy particles. As noted in a previous section, these authors have emphasized the importance of solar wind–driven convective transport at Uranus [*Vasyliunas*, 1986; *Selesnick and Richardson*, 1986; *McNutt et al.*, 1987; *Hill*, 1986; *Selesnick and McNutt*, this issue]. Global convective time scales ranging from tens of hours to a week have been estimated. In the present work we have suggested that dynamical earthlike substorm processes play important roles in the transport of particles within and at the base of the magnetotail. In many respects, global convection and substorm processes constitute

two sides of the same coin, since it is likely that substorms are a response to the stresses inherent in the global convective reconfiguration of the magnetosphere [e.g., *Schindler and Birn*, 1982]. However, the question of the relative roles of dynamical versus quasi-time-stationary transport is an important one at Uranus, since that question remains quite controversial with respect to the Earth's magnetosphere [e.g., *Kivelson et al.*, 1987]. A comparative magnetospheric approach, particularly when the comparison is between a relatively high β and a relatively low β magnetosphere, is particularly attractive.

As described earlier, a principal issue concerning low-energy particle transport is the interpretation of the sharp inner edge cutoffs in the "hot" plasma component observed by the Voyager PLS team (particle energies <6 keV [*McNutt et al.*, 1987]). These cutoffs have been interpreted [*McNutt et al.*, 1987; *Selesnick and McNutt*, this issue] as being generated by a dramatic shielding of the solar wind–generated convection electric field near the position of the cutoffs. This model has been presented as a natural analog to the workings of the Earth's magnetosphere. We will emphasize here that that model is by no means generally accepted with regard to the Earth's magnetosphere (see also *Mauk and Zanetti* [1987]).

Strong evidence has been presented that within the Earth's magnetosphere, plasma cutoffs are not caused by the quasi-time-stationary, shielded convection but rather by strongly dynamical processes that involve localized inductive effects [*Mauk and Meng*, 1983, 1986; *Newell and Meng*, 1987]. From a theoretical standpoint it has been shown that because of boundary value constraints on the magnetosphere, quasi-time-stationary convection from the tail to the inner regions cannot occur [*Erickson and Wolf*, 1980; *Schindler and Birn*, 1982]. With regard to the shielding of the global electric field, observations show that more often than not the region 2 field-aligned currents, responsible for carrying the shielding charges at Earth, are closed within the central plasma sheet regions and not at the inner edge of the plasma sheet population [*Klumpar et al.*, 1976; *Robinson*, 1984; *Sugiura et al.*, 1984]. Pressure gradients measured by *Lui et al.* [1987] and inferred by *Roux et al.* [1986] suggest that over radial scale sizes observationally attributed to the region 2 system at Earth (>3 R_E), the total pressure gradient points toward the planet and not away from the planet, as is required by the simple shielding models. More recently, *Caudal* [1987] has shown that the region 2 currents are not generated by the usually proposed mechanism (i.e., a radially outward pressure gradient). Finally, extensive observations of plasma dispersions near the inner edge of the plasma sheet at Earth have shown that in all likelihood the earthward transport of these particles is always associated with impulsive, relatively localized, and inductively driven processes which work together with the global convection to cause the transport [*Mauk and Meng*, 1986].

Our observations, both in the Uranian magnetotail and within the quasi-dipolar regions of the Uranian magnetosphere, suggest an analogy to the dynamical characteristics of the Earth's magnetosphere. We suggest that the sharp spatial boundaries might more naturally be attributed to the same type of dynamical substorm processes that generate sharp spatial boundaries within the Earth's magnetosphere. Very extreme shielding would not be required (and is not generally observed at Earth [*Mauk and Zanetti*, 1987]). *McNutt et al.* [1987] did suggest that "substorm" time variations might have produced some of the observed features near the inner edge boundary. However, on the basis of the Earth analogy, we suggest a much more important role for the substorm processes at Uranus.

REFERENCES

Armstrong, T. P., and S. M. Krimigis, Observations of protons in the magnetosphere and magnetotail with Explorer 33, *J. Geophys. Res.*, 73, 143, 1968.

Armstrong, T. P., M. T. Paonessa, S. I. Brandon, S. M. Krimigis, and L. J. Lanzerotti, Low-energy charged particle observations in the 5–20 R_J region of the Jovian magnetosphere, *J. Geophys. Res.*, 86, 8343, 1981.

Armstrong, T. P., M. T. Paonessa, E. V. Bell II, and S. M. Krimigis, Voyager observations of Saturnian ion and electron phase space densities, *J. Geophys. Res.*, 88, 8893, 1983.

Behannon, K. W., R. P. Lepping, E. C. Sittler, N. F. Ness, B. H. Mauk, S. M. Krimigis, and R. L. McNutt, The magnetotail of Uranus, *J. Geophys. Res.*, this issue.

Block, L., Three-dimensional potential structure associated with Birkeland currents, in *Magnetospheric Currents, Geophys. Monogr. Ser.*, vol. 28, edited by T. A. Potemra, p. 315, AGU, Washington, D. C., 1984.

Bridge, H. S., et al., Plasma observations near Uranus: Initial results from Voyager 2, *Science*, 233, 89, 1986.

Carbary, J. F., S. M. Krimigis, E. P. Keath, G. Gloeckler, W. I. Axford, and T. P. Armstrong, Ion anisotropies in the outer Jovian magnetosphere, *J. Geophys. Res.*, 86, 8285, 1981.

Caudal, G., Field-aligned currents deduced from EISCAT radar observations and implications concerning the mechanism that produces region 2 currents, *J. Geophys. Res.*, 92, 6000, 1987.

Cheng, A. F., Proton and oxygen plasmas at Uranus, *J. Geophys. Res.*, this issue.

Cheng, A. F., S. M. Krimigis, B. H. Mauk, E. P. Keath, C. G. Maclennan, L. J. Lanzerotti, M. T. Paonessa, and T. P. Armstrong, Energetic ion and electron phase space densities in the magnetosphere of Uranus, *J. Geophys. Res.*, this issue.

Connerney, J. E. P., M. H. Acuña, and N. F. Ness, The magnetic field of Uranus, *J. Geophys. Res.*, this issue.

Eastman, T. E., L. A. Frank, W. K. Peterson, and W. Lennartsson, The plasma sheet boundary layer, *J. Geophys. Res.*, 89, 1553, 1984.

Erickson, G. M., and R. A. Wolf, Is steady convection possible in the earth's magnetotail?, *Geophys. Res. Lett.*, 7, 897, 1980.

Gurnett, D. A., W. S. Kurth, F. L. Scarf, and R. L. Poynter, First plasma wave observations at Uranus, *Science*, 233, 106, 1986.

Hamilton, D. C., G. Gloeckler, S. M. Krimigis, and L. J. Lanzerotti, Composition of nonthermal ions in the Jovian magnetosphere, *J. Geophys. Res.*, 86, 8301, 1981.

Hess, W. N., and G. D. Mead, The boundary of the magnetosphere, in *Introduction of Space Science*, edited by W. N. Hess, Gordon and Breach, New York, 1965.

Hill, T. W., Solar-wind interaction with the magnetospheres of Uranus, paper presented at 2nd Neil Brice Memorial Symposium on Magnetospheres of the Outer Planets, Dep. of Phys. and Astron., Univ. of Iowa, Iowa City, Iowa, Sept. 1–5, 1986.

Kennel, C. F., and H. E. Petschek, Limit on stably trapped particle fluxes, *J. Geophys. Res.*, 71, 1, 1966.

Kivelson, M. G., J. Feynman, B. H. Mauk, and R. A. Wolf, Dialogue on injection boundary versus Alfvén-layer models, in *Magnetotail Physics*, edited by A. T. Y. Lui, p. 403, Johns Hopkins University Press, Baltimore, Md., 1987.

Klumpar, D. M., J. R. Burrows, and M. D. Burrows, Simultaneous observations of currents and particle fluxes in the post-midnight sector, *Geophys. Res. Lett.*, 3, 395, 1976.

Krimigis, S. M., T. P. Armstrong, W.-I. Axford, C. O. Bostrom, C. Y. Fan, G. Gloeckler, and L. J. Lanzerotti, The low energy charged particle (LECP) experiment on the Voyager spacecraft, *Space Sci. Rev.*, 21, 329, 1977.

Krimigis, S. M., T. P. Armstrong, W. I. Axford, C. O. Bostrom, C. Y. Fan, G. Gloeckler, L. J. Lanzerotti, E. P. Keath, R. D. Zwickl, J. F. Carbury, and D. C. Hamilton, Low-Energy Charged Particle environment at Jupiter: A first look, *Science*, *204*, 998, 1979.

Krimigis, S. M., J. F. Carbary, E. P. Keath, C. O. Bostrom, W. I. Axford, G. Gloeckler, L. J. Lanzerotti, and T. P. Armstrong, Characteristics of hot plasma in the Jovian magnetosphere: Results from the Voyager spacecraft, *J. Geophys. Res.*, *86*, 8227, 1981.

Krimigis, S. M., J. F. Carbary, E. P. Keath, T. P. Armstrong, L. J. Lanzerotti, and G. Gloeckler, General characteristics of hot plasma and energetic particles in the Saturnian magnetosphere; Results from the Voyager spacecraft, *J. Geophys. Res.*, *88*, 8871, 1983.

Krimigis, S. M., T. P. Armstrong, W. I. Axford, A. F. Cheng, G. Gloeckler, D. C. Hamilton, E. P. Keath, L. J. Lanzerotti, and B. H. Mauk, The magnetosphere of Uranus: Hot plasma and radiation environment, *Science*, *233*, 97, 1986.

Lanzerotti, L. J., C. G. Maclennan, R. P. Lepping, and S. M. Krimigis, On the plasma conditions at the dayside magnetopause of Saturn, *Geophys. Res. Lett.*, *10*, 1209, 1983.

Lanzerotti, L. J., W. L. Brown, C. G. Maclennan, A. F. Cheng, S. M. Krimigis, and R. E. Johnson, Effects of charged particles on the surfaces of the satellites of Uranus, *J. Geophys. Res.*, this issue.

Lui, A. T. Y., R. W. McEntire, and S. M. Krimigis, Evolution of the ring current during two geomagnetic storms, *J. Geophys. Res.*, *92*, 7459, 1987.

Maclennan, C. G., L. J. Lanzerotti, S. M. Krimigis, and R. P. Lepping, Low-energy particles at the bow shock, magnetopause, and outer magnetosphere of Saturn, *J. Geophys. Res.*, *88*, 8817, 1983.

Mauk, B. H., and C.-I. Meng, Dynamical injections as the source of near geostationary quiet-time particle spatial boundaries, *J. Geophys. Res.*, *88*, 10011, 1983.

Mauk, B. H., and C.-I. Meng, Macroscopic ion acceleration associated with the formation of the ring current in the earth's magnetosphere, in *Ion Acceleration in the Magnetosphere and Ionosphere*, *Geophys. Monogr. Ser.*, vol. 38, edited by T. Chang, p. 351, AGU, Washington, D. C., 1986.

Mauk, B. H., and L. J. Zanetti, Magnetospheric electric fields and currents, *Rev. Geophys.*, *25*, 541, 1987.

McNutt, R. L., Jr., Force balance in the outer planet magnetospheres, in *Proceedings of the 1982–4 Symposium on the Physics of Space Plasmas*, *SPI Conf. Proc. Reprint Ser. 5*, edited by H. Bridge, J. W. Belcher, T. S. Chang, B. Coppi, and J. R. Jasperse, Scientific Publishers, Cambridge, Mass., 1984.

McNutt, R. L., Jr., R. S. Selesnick, and J. D. Richardson, Low-energy plasma observations in the magnetosphere of Uranus, *J. Geophys. Res.*, *92*, 4399, 1987.

Meng, C.-I., and K. L. Anderson, A layer of energetic electrons (>40 keV) near the magnetopause, *J. Geophys. Res.*, *75*, 1827, 1970.

Meng, C.-I., L. A. Frank, and K. L. Anderson, Particle and field characteristics of the dayside magnetopause energetic electron layer, Magnetospheric Boundary Layers, *Eur. Space Agency Spec. Publ., SP-148*, 143, 1979.

Mitchell, D. G., Kinetic aspects of magnetotail observations, in *Magnetotail Physics*, edited by A. T. Y. Lui, p. 207, Johns Hopkins University Press, Baltimore, Md., 1987.

Mitchell, D. G., R. Lundin, and D. J. Williams, Analysis of convective flow and spatial gradients in energetic proton observations, *J. Geophys. Res.*, *91*, 8827, 1986.

Ness, N. F., M. H. Acuña, K. W. Behannon, L. F. Burlaga, J. E. P.

Connerney, R. P. Lepping, and F. M. Neubauer, Magnetic fields at Uranus, *Science*, *233*, 85, 1986.

Newell, P. T., and C.-I. Meng, Energy dependence of the equatorward cutoffs in auroral electron and ion precipitation, *J. Geophys. Res.*, *92*, 7519, 1987.

Northrop, T. G., T. J. Birmingham, and A. W. Schart, Anisotropies in fluxes of Pioneer 10 protons, *J. Geophys. Res.*, *84*, 47, 1979.

Paonessa, M., and A. F. Cheng, Satellite sweeping in offset, tilted dipole fields, *J. Geophys. Res.*, *92*, 1160, 1987.

Robinson, R. M., Coordinated ground and satellite observations of conductivities, electric fields, and field-aligned currents, in *Magnetospheric Currents*, *Geophys. Monogr. Ser.*, vol. 28, edited by T. A. Potemra, p. 192, AGU, Washington, D. C., 1984.

Roelof, E. C., E. P. Keath, C. O. Bostrom, and D. J. Williams, Fluxes of ≥ 50-keV protons and ≥ 30-keV electrons at ~ 35 R_E, 1, Velocity anisotropies and plasma flow in the magnetotail, *J. Geophys. Res.*, *81*, 2304, 1976.

Roux, A., S. Perraut, A. Pedersen, R. Dellinex, and D. Rodgers, Instability of the plasma sheet in relation to substorms, paper presented to Sixth International Symposium on Solar-Terrestrial Physics, Spec. Comm. for Sol.-Terr. Phys., Toulouse, France, June 30 to July 5, 1986.

Schindler, K., and J. Birn, Self-consistent theory of time-dependent convection in the earth's magnetotail, *J. Geophys. Res.*, *87*, 2263, 1982.

Selesnick, R. S., and R. L. McNutt, Jr., Voyager 2 plasma ion observations in the magnetosphere of Uranus, *J. Geophys. Res.*, this issue.

Selesnick, R. S., and J. D. Richardson, Plasmasphere formation in arbitrary oriented magnetospheres, *Geophys. Res. Lett.*, *13*, 624, 1986.

Stone, E. C., J. F. Cooper, A. C. Cummings, F. B. McDonald, J. H. Trainor, N. Lal, R. McGuire, and D. L. Chenette, Energetic charged particles in the Uranian magnetosphere, *Science*, *233*, 93, 1986.

Sugiura, M., T. Iyemori, R. A. Hoffman, N. C. Maynard, J. L. Burch, and J. D. Winningham, Relationship between field-aligned currents, electric fields, and particle precipitation as observed by Dynamics Explorer-2, in *Magnetospheric Currents*, *Geophys. Monogr. Ser.*, vol. 28, edited by T. A. Potemra, p. 96, AGU, Washington, D. C., 1984.

Vasyliunas, V. M., The convection dominated magnetosphere of Uranus, *Geophys. Res. Lett.*, *13*, 621, 1986.

Williams, D. J., Energetic ion beams at the edge of the plasma sheet: ISEE 1 observations plus a simple explanatory model, *J. Geophys. Res.*, *86*, 5507, 1981.

T. P. Armstrong, Department of Physics, University of Kansas, Lawrence, KS 66044.

A. F. Cheng, E. P. Keath, S. M. Krimigis, and B. H. Mauk, Applied Physics Laboratory, Johns Hopkins University, Laurel, MD 20707.

G. Gloeckler and D. C. Hamilton, Department of Physics and Astronomy, University of Maryland, College Park, MD 20742.

L. J. Lanzerotti, AT&T Bell Laboratories, MS IE-439, 600 Mountain Avenue, Murray Hill, NJ 07974.